THESIS FOR THE DEGREE OF LICENTIATE OF PHILOSOPHY

Charting Circumstellar Chemistry of Carbon-rich AGB Stars

Ramlal Unnikrishnan

CHALMERS
UNIVERSITY OF TECHNOLOGY

Astronomy and Plasma Physics Division
Department of Space, Earth and Environment
Chalmers University of Technology
Gothenburg, Sweden, 2023

Charting Circumstellar Chemistry of Carbon-rich AGB Stars

Ramlal Unnikrishnan

Astronomy and Plasma Physics Division
Department of Space, Earth and Environment
Chalmers University of Technology
SE-412 96 Gothenburg, Sweden
Phone: +46 (0)31 772 1000
www.chalmers.se

Contact information:
Ramlal Unnikrishnan
Onsala Space Observatory
Chalmers University of Technology
SE-439 92 Onsala, Sweden
Phone: +46 (0)31 772 5544
Email: ramlal.unnikrishnan@chalmers.se

Cover image: *'Drawing of ALMA'*, Emma Sakurako Tafoya Sato, 2023

This thesis has been prepared using LaTeX

Printed by Chalmers Reproservice
Gothenburg, Sweden, March 2023

Abstract

Stars of low to intermediate initial masses (0.8 - 8 $M_{\odot}$) enter the asymptotic giant branch (AGB) phase during their late evolution. This phase is characterised by intense mass loss from the stellar surface into the interstellar medium (ISM), eventually leading to the formation of an extended circumstellar envelope (CSE) composed of the ejected gas and dust around the star. These stars are also the birthplace of many heavy elements. AGB stars thus contribute heavily to the chemical replenishment of the ISM in galaxies, by enriching it with the nuclear-processed material dredged up from the stellar interiors. This makes AGB CSEs very interesting cosmic chemical laboratories, sites of diverse, and often complex chemistry.

Based on the relative abundances of carbon and oxygen in their atmospheres, AGB stars are categorised into C-rich and O-rich, the carbon stars being more chemically complex than their oxygen-rich counterparts. The study of molecular line emission from AGB CSEs is of particular interest, as it can help constrain both the physical and chemical characteristics of the envelopes. However, much of our current knowledge of AGB circumstellar chemistry, particularly of the C-rich type, is based on observations and models of a single object, IRC+10 216, which is often regarded as an archetypical carbon star. Advances in instrumentation, including the development of high angular resolution interferometers, have opened up possibilities for observational studies of additional sources in unprecedented detail.

This thesis summarises our current understanding of the chemistry in C-rich CSEs, and presents the first spatially-resolved, unbiased spectral surveys of the circumstellar molecular emission from multiple carbon stars other than IRC +10 216. ALMA band 3 spectral surveys of three C-rich AGB stars reveal the morphological and chemical complexity of their CSEs. We compare the results obtained from these surveys with those of IRC +10 216, and discuss their implications for the generalised understanding of the chemistry in carbon star CSEs. By obtaining well-constrained estimates of the emission region sizes and circumstellar abundances of a variety of molecular species, this work aims to provide updates to existing chemical models, and put to test the archetype status attributed to IRC +10 216 in the literature.

Keywords: Stars: AGB and post-AGB – stars: mass-loss – stars: winds, outflows – circumstellar matter – submillimeter: stars – astrochemistry.

"There is no royal road to science, and only [...] the fatiguing climb of its steep paths can gain its luminous summits."

– Marx, *Capital Vol. I*[1]

Many thanks to everyone who helped me navigate the fatiguing climb of reducing our ALMA data.

[1] Marx, K. (1872), *Capital: A critique of political economy, Volume I, preface to the first French edition (Le Capital: Critique de l'économie politique, préface à la première édition française)*, Maurice Lachâtre, Paris.

List of Publications

This thesis is based on the following publication:

[A] **R. Unnikrishnan**, E. De Beck, L. -Å. Nyman, H. Olofsson, W. H. T. Vlemmings, D. Tafoya, M. Maercker, S. B. Charnley, M. A. Cordiner, I. de Gregorio, E. Humphreys, T. J. Millar, and M. G. Rawlings, *"Charting circumstellar chemistry of carbon-rich AGB stars I. ALMA 3 mm spectral surveys"*, Submitted to Astronomy & Astrophysics.

Other publications by the author, not included in this thesis:

- D. Tafoya, J. A. Toalá, **R. Unnikrishnan**, W. H. T. Vlemmings, M. A. Guerrero, S. Kimeswenger, P. A. M. van Hoof, L. A. Zapata, S. P. Treviño-Morales, and J. B. Rodríguez-González, *"First images of the molecular gas around a born-again star revealed by ALMA"*, ApJL 925 L4, January 2022.

Acknowledgements

There is a long list of people who have contributed in various ways to this project, and have helped and supported me a lot during this first half of the Ph.D. journey.

First and foremost, I want to thank my supervisor, Dr. Elvire De Beck, for simply being the best Ph.D. supervisor one could ever imagine working with, far exceeding the expectations of supervision I had before taking up this position. You have taught me a lot of wonderful science, and always addressed my every little doubt and question, with never-ending patience. You have always made sure to ensure that the work is proceeding smoothly, and that I am comfortable and stress-free during the process. You have also contributed greatly to my overall development as a researcher, be it by encouraging me to attend various workshops and conferences, or by sending me to Chile for observations, to name a few things. Thank you, Elvire, from the bottom of my heart, for guiding me these past two and a half years. I look forward, with a lot of happiness and excitement, to working with you on the next half of my doctoral research.

Next, I would like to thank Dr. Lars-Åke Nyman and Prof. Hans Olofsson. Both of you inspire me every day, and I consider it a great honour and privilege to be called your student. Lars, I can never thank you enough for always finding the time to help me out with the project, even from continents apart. Your unmatched dedication and brilliant insights form the foundation of this project. Thanks for taking me around in Chile as well. Hans, thanks a lot for your expert advice and exemplary guidance throughout, and for helping me navigate the writing of my first research paper. My thanks to Dr. Matthias Maercker, for being an amazing co-supervisor and line manager. You strive tirelessly to ensure that the work environment is continuously improved for all of us. You make AoP a better place, and I am very grateful to you for that. In addition, your motivation, and constant reassurance that the project is going well, have helped me manage the pressure of academic research and continue onwards on several occasions. My sincere gratitude also to Prof. Wouter Vlemmings, for being my Ph.D. examiner, and for the many spontaneous discussions even amidst his busy schedule. His valuable comments and suggestions have significantly improved this thesis and the attached paper.

I do not have words to express my sincere gratitude to my dear friend and mentor Dr. Daniel Tafoya. Daniel, you have been an amazing teacher, perhaps

even the best I ever had, and simultaneously one of my closest friends. I shall forever cherish our countless random conversations, scientific and otherwise, little moments of frustration and breakthroughs during the data processing days, and our many long fikas and dinners. You share, to the same extent or probably more, my childish curiosity towards space and astronomy. Thank you, for allowing me to depend on you, and for being there every single time, without exception. I could not have done this without you. Here is to having fun exploring the universe together.

Next, I would like to thank my friend, office mate, and fellow Ph.D. student Behzad Bojnordi Arbab. Behzad, I shall always treasure the moments of knowledge and fun we share, be it at the office, the ping-pong table, or during our travels. Many thanks to you for finding time to teach me bits and pieces of your immensely beautiful language, Persian, as well. I could never have asked for a better office mate. I also want to thank my close friends and colleagues Asnakew Bewketu Belete and Mamiko Sato. The bond I share with you both is something I consider invaluable, and it is a pleasure and relief to share a department with you. I am grateful to Miora Andriantsaralaza for being my good friend and also for helping out with the project. I also thank all Ph.D. students and colleagues at AoP and OSO.

I thank all my family and friends, both in India and Sweden, for their constant support and encouragement. Finally, above all else, I thank my beloved parents, whose unwavering and unconditional love and support is the primary reason I am able to pursue this career, and everything else in my life. Wherever I go, home will always be where you both are, and not a day goes by when I do not long to get back to you.

Ramlal Unnikrishnan
Göteborg, April 2023

List of Abbreviations

HR	Hertzsprung-Russell
MS	Main Sequence
RGB	Red Giant Branch
HB	Horizontal Branch
AGB	Asymptotic Giant Branch
E-AGB	Early Asymptotic Giant Branch
TP-AGB	Thermally Pulsing Asymptotic Giant Branch
WD	White dwarf
HBB	Hot Bottom Burning
FDU	First dredge-up
SDU	Second dredge-up
TDU	Third dredge-up
SR	Semi-regular
LPV	Long-period Variable
MLR	Mass Loss Rate
CSE	Circumstellar Envelope
ISM	Interstellar Medium
ALMA	Atacama Large Millimeter/submillimeter Array
ACA	Atacama Compact Array
APEX	Atacama Pathfinder EXperiment
SKA	Square Kilometre Array
IRAM	Institut de Radioastronomie Millimetrique
NOEMA	Northern Extended Millimeter Array
IRC	Infrared Catalog
ESO	European Southern Observatory
NRAO	National Radio Astronomy Observatory
pp	proton-proton
CNO	Carbon-Nitrogen-Oxygen
DARWIN	Dynamical Atmospheres and Radiation-driven Wind models with Implicit Numerics
FIR	Far-infrared
IRAS	Infrared Astronomical Satellite
CDMS	Cologne Database for Molecular Spectroscopy
ISRF	Interstellar Radiation Field

HIFI : Heterodyne Instrument for the Far-Infrared
PAH : Polycyclic Aromatic Hydrocarbon
SEST : Swedish-ESO Submillimeter Telescope
PWV : Precipitable Water Vapor
JWST : James Webb Space Telescope
LO : Local Oscillator
IF : Intermediate Frequency
SIS : Superconductor-Insulator-Superconductor
SSB : Single Side Band
DSB : Double Side Band
2SB : Dual Side Band
MB : Main Beam
LTE : Local Thermodynamic Equilibrium
AFGL : Air Force Geophysical Laboratory

Mathematical symbols

$M_\odot$: Solar mass
$R_\odot$: Solar radius
$L_\odot$: Solar luminosity
$M_\star$: Birth mass of the star
θ_{res} : Angular resolution
λ : Wavelength
ν : Frequency
Ω : Solid angle

Contents

List of Figures

List of Tables

Outline of the thesis

This thesis, titled *Charting Circumstellar Chemistry of Carbon-rich AGB Stars*, provides the necessary astrophysical and chemical background, both theoretical and observational, for the research work presented in the appended paper **??**. Paper **??** is the first in a series of planned publications, which are together structured to approach the question of carbon-chemistry in AGB CSEs using multiple tools, including observations, radiative transfer analysis, and chemical modelling.

Chapter 1 offers a general introduction to stars and stellar evolution, while Chapter 2 delves into asymptotic giant branch (AGB) stars specifically. Their physical structure and evolution are discussed, and the mass loss process leading to the formation of the circumstellar envelope (CSE) is explained. The scientific relevance of the study of AGB stars is also explored, in the context of their contribution to nucleosynthesis and galactic chemical replenishment.

In Chapter 3, the physics of molecular transitions and emission line spectra is outlined, and their capacity as excellent diagnostic tools to explore the physical conditions and chemical evolution of astronomical sources including AGB CSEs is looked into. The benefits offered by unbiased spectral surveys of molecular line emission, in use cases like those of this work, are laid out.

Chapter 4 explores in some detail the chemistry in the circumstellar envelopes of AGB stars. The molecules detected to date in circumstellar environments are listed. The chemical classification of AGB stars, and the vari-

ous processes influencing circumstellar chemistry are discussed. This chapter briefly summarises the existing knowledge on the chemistry of carbon-rich CSEs, based on observations and models available in the literature. The context of, and need for this particular project are then delineated by situating the goals of paper **??** within the context of our current understanding of these objects.

Observational techniques and instrumentation used to obtain the data used in this project are described in Chapter 5. The calibration and data reduction methods employed are also briefly mentioned. Chapter 6 summarises paper **??**, highlighting the aims, methodology, main results and conclusions of the work. Finally, Chapter 7 outlines the plans for the upcoming work, and the outlook for future projects.

1

Introduction

"The stars are the landmarks of the universe."
– John Herschel

1.1 Stars

Stars are some of the most fascinating objects in the universe, from the perspective of both fundamental physics and human culture. The sparkling dots in the night sky have inspired emotions of awe, wonder, and curiosity in humans across the globe, from time immemorial. They have stimulated poetry and romance, fostered fateful superstitions, and have been the subject of countless myths and legends across civilizations. Societies from all parts of the world gave birth to great folklore and beautiful stories by ascribing familiar shapes and patterns to groups of stars, a practice we have joyfully kept alive to date. At the same time, stars have also been objects of great scientific relevance and intensive study for centuries, and have played a crucial role in time reckoning, and in the development of agriculture, navigation, and much

more. The history of the study of stars is thus the history of the progress of mankind, from the hunter-gatherer to the modern human.

It is the energy from our star, the Sun, that is exclusively responsible for the sustenance of all life on Earth. Stars are responsible for the production of all elements heavier than helium, and a large part of the radiation in the universe. They are also the drivers of the physical and chemical evolution of galaxies and thereby the universe itself. Inevitably, research on the formation, structure, and evolution of stars plays a central role in the continuous development of modern-day astronomy and astrophysics, and is pivotal to understanding our origin and place in the universe.

There are hundreds of billions of stars in our galaxy, the Milky Way, itself. Most of them, including our Sun, are of relatively low or intermediate masses, ranging from around 0.8 to 8 $M_{\odot}$. Over billions of years, these stars will eventually evolve into a phase called the *asymptotic giant branch* (AGB). AGB stars are the sites of production of a large variety of elements, including carbon and oxygen which are crucial for the origin and maintenance of life on Earth. Their circumstellar envelopes (see Sect. 2.5) are also rich sites of molecule and dust formation. AGB stars contribute significant amounts of gas and dust to the surrounding interstellar medium (see Sect. 2.6). The study of the physics, chemistry, and evolution of these stars is therefore of great significance in understanding the chemical evolution of the universe. The main focus of this thesis is on the molecular chemistry in the circumstellar envelopes of AGB stars.

1.2 The life cycle of stars

The contents of this section are broadly based on Lattanzio & Wood, in Habing & Olofsson (2003), which serves as the general reference wherever other literature is not explicitly cited.

The evolutionary trajectory of a star is primarily determined by its initial mass, although other factors, including the presence of companion stars, and initial metallicity (abundance of elements heavier than helium), also play major roles. Stars are formed by the fragmentation and collapse of dense molecular clouds. These clouds collapse under the effect of their own gravity, until their central regions reach temperatures and pressures high enough to

initiate hydrogen fusion, which is the point we denote as the *birth* of a star. A detailed review of the star formation process and related phenomena is outside the scope of this thesis. The interested reader is referred to Stahler & Palla (2004); McKee & Ostriker (2007); Ward-Thompson & Whitworth (2011); or Bodenheimer (2011).

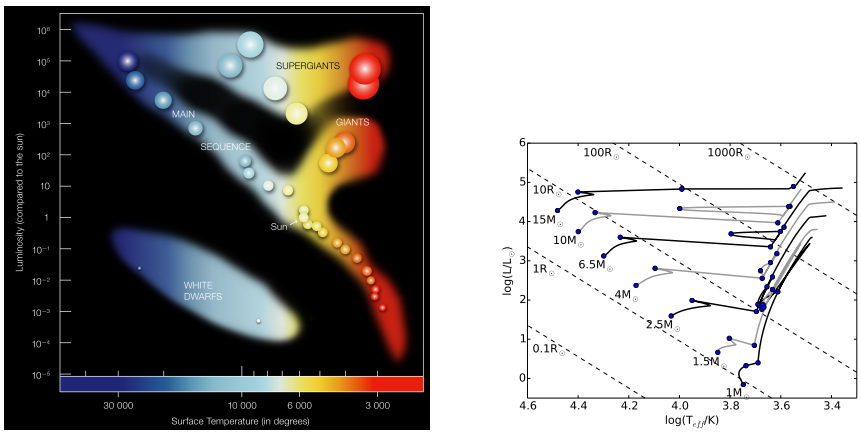

(a) HR diagram **(b)** Evolutionary tracks

Figure 1.1: (a) Schematic view of the HR diagram, showing the different phases in stellar evolution (credit: ESO). (b) Evolutionary tracks of 1 - 10 $M_\odot$ stars in the HR diagram (credit: Toonen et al. 2016).

The various phases in the evolution of a star are named according to the position of the star in each phase in a plot of luminosity vs surface temperature. Such a plot is known as the *Hertzsprung-Russell diagram* (HR diagram, see Fig. 1.1a). The HR diagram is a fundamental tool in the study of stellar evolution, developed in the early 1900s by astronomers Ejnar Hertzsprung and Henry Norris Russell. The path traced by a star in the HR diagram as it evolves is called its *evolutionary track*. The evolutionary tracks of stars of initial masses in the range 1 - 15 $M_\odot$ are shown in Fig. 1.1b, and Fig. 1.2 zooms into the evolutionary track of a 1 $M_\odot$ star, and the various phases in its evolution.

The sections below briefly outline the characteristics of the various evolutionary stages of a low/intermediate mass ($0.8\ M_\odot < M_\star < 8\ M_\odot$) star, starting from its birth. See Kippenhahn & Weigert (1990), and Lamers &

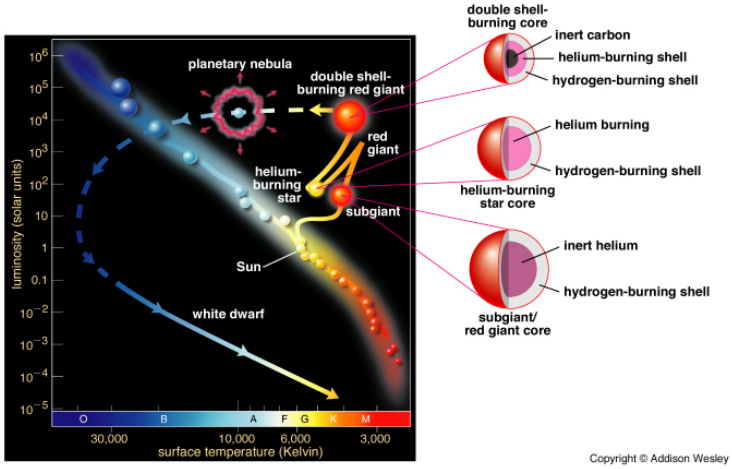

Figure 1.2: The evolutionary track of a 1 $M_\odot$ star in the HR diagram, showing the stellar structure at various phases (credit: Pearson Education).

Levesque (2017) for detailed descriptions of the physics and phases of stellar evolution.

1.2.1 Pre-AGB evolution

1.2.1.1 Main sequence

The *main sequence* (MS) phase is the first and longest stage in the evolution of stars, It is the long strip running diagonally across the HR diagram (Fig. 1.1a), from the high luminosity and temperature region at the top-left to the low luminosity, cool region at the bottom right. The time spent by a star in this phase is dependent on its initial mass. The lower the mass of the star, the more time it spends on the MS. While a star of $\sim$0.1 $M_\odot$ takes roughly 10^{12} years (more than the current age of the universe) to complete its MS evolution, a massive star of $\sim$60 $M_\odot$ will only spend 10^6 years in the main sequence.

In this phase, the star releases energy by fusing the hydrogen in its core to helium. The reaction pathway by which this fusion occurs also depends on the birth mass ($M_\star$) of the star. For stars with $M_\star < 1.3$ $M_\odot$ (see Salaris & Cassisi 2005), the hydrogen fusion is dominated by the *proton-proton* (pp)

chain. The reaction sequence for the pp chain is as follows:

$$\begin{cases} {}^1\mathrm{H} + {}^1\mathrm{H} & \longrightarrow {}^2\mathrm{H} + \mathrm{e}^+ + \nu_e \\ {}^2\mathrm{H} + {}^1\mathrm{H} & \longrightarrow {}^3\mathrm{He} + \gamma \\ {}^3\mathrm{He} + {}^3\mathrm{He} & \longrightarrow {}^4\mathrm{He} + 2\,{}^1\mathrm{H} \end{cases} \tag{1.1}$$

where e^+ denotes a positron, ν_e is an electron neutrino, and γ is a gamma particle. The formation of ^{4}He as per the third reaction in Eq. 1.1, is referred to as the pp1 chain. Fig. 1.3 shows the schematic view of H-fusion through the pp1-chain. At different temperatures, other proton-proton chains (pp2 and pp3) can be activated, which lead to the production of heavier elements Li and Be in addition to ^{4}He. See LeBlanc (2010) for the details of these less-frequent pathways.

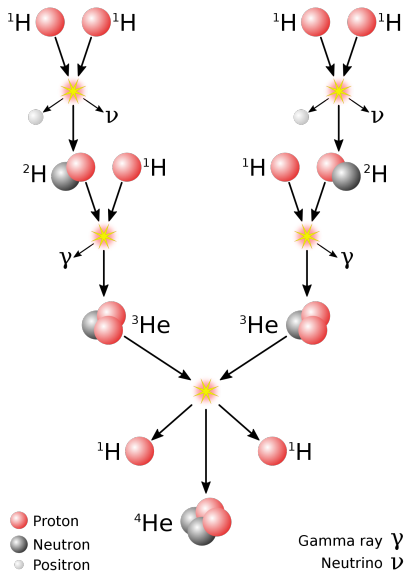

Figure 1.3: Schematic view of the pp1-chain, showing the formation of ^{4}He by H-fusion (credit: *Wikipedia*[1]).

For stars having $M_\star > 1.3\ M_\odot$, the *carbon-nitrogen-oxygen* (CNO) cycle dominates the H-burning. The reactions involved in the major branch of the

[1] https://en.wikipedia.org/wiki/Proton-proton_chain

CNO cycle are:

$$\begin{cases} {}^{12}\mathrm{C} + {}^{1}\mathrm{H} \longrightarrow {}^{13}\mathrm{N} + \gamma \\ {}^{13}\mathrm{N} \longrightarrow {}^{13}\mathrm{C} + \mathrm{e}^{+} + \nu_e \\ {}^{13}\mathrm{C} + {}^{1}\mathrm{H} \longrightarrow {}^{14}\mathrm{N} + \gamma \\ {}^{14}\mathrm{N} + {}^{1}\mathrm{H} \longrightarrow {}^{15}\mathrm{O} + \gamma \\ {}^{15}\mathrm{O} \longrightarrow {}^{15}\mathrm{N} + \mathrm{e}^{+} + \nu_e \\ {}^{15}\mathrm{N} + {}^{1}\mathrm{H} \longrightarrow {}^{12}\mathrm{C} + {}^{4}He \end{cases} \tag{1.2}$$

and

$$\begin{cases} {}^{15}\mathrm{N} + {}^{1}\mathrm{H} \longrightarrow {}^{16}\mathrm{O} + \gamma \\ {}^{16}\mathrm{O} + {}^{1}\mathrm{H} \longrightarrow {}^{17}\mathrm{F} + \gamma \\ {}^{17}\mathrm{F} \longrightarrow {}^{17}\mathrm{O} + \mathrm{e}^{+} + \nu_e \\ {}^{17}\mathrm{O} + {}^{1}\mathrm{H} \longrightarrow {}^{14}\mathrm{N} + +{}^{4}He \end{cases} \tag{1.3}$$

The reactions in Eq. 1.2 constitute the CN cycle, shown schematically in Fig. 1.4. Eq. 1.2 and 1.3 together form the CNO cycle. The CNO cycle produces ^{14}N as a byproduct, and is relevant to the hot bottom burning process (see Sect. 2.3.2.4) in the AGB phase as well, in addition to the core hydrogen fusion in the main sequence phase.

1.2.1.2 Red Giant Branch and Horizontal Branch

Once the star has exhausted the hydrogen in its core by converting it to helium, the core contracts due to the absence of radiation pressure to balance self-gravity. As the core contracts, the outer layers of the star expand, increasing the stellar radius ($R_\star$) more than an order of magnitude in a timescale of roughly a million years. A layer of hydrogen in a shell above the core will reach temperatures sufficient enough to initiate hydrogen fusion, which now becomes the source of energy production in the star. The expanded star is now a *red giant*, and this phase in the HR diagram is called the red-giant branch (RGB). This stage is characterised by an inert helium core surrounded by shell burning of hydrogen. As the outer layers expand and cool, the luminosity of the star rises to more than 100 times the solar luminosity. During this phase, large convective motions will move nucleosynthetic products from the internal layers to the surface of the star, in a process known as the *first dredge-up* (see

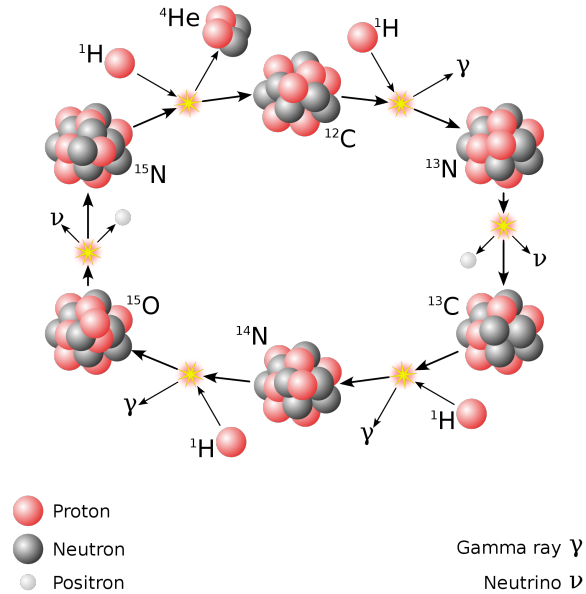

Figure 1.4: Schematic view of the CNO cycle, showing the formation of ^{4}He by H-fusion (credit: *Wikipedia*[2]).

Sect. 2.3.2.3).

The shell-burning of hydrogen continues to produce more and more helium as the star ascends the RGB, increasing the mass and temperature of the helium core. For low-mass ($0.8\ M_\odot < M_\star < 2\ M_\odot$) stars, helium fusion is initiated at the tip of the RGB in a thermal-runaway process called the *helium flash* which rapidly raises the core temperature ($\sim 10^8$ K) and lifts its degeneracy. The star now enters the *horizontal branch* (HB). The HB is characterised by a helium-fusing core surrounded by a shell of hydrogen burning.

Helium burning in the core of HB stars occurs through the *triple-alpha* process, where three helium nuclei are fused to form one carbon nucleus. The reactions involved in the triple-alpha process are given below, and are shown schematically in Fig. 1.5.

[2] https://en.wikipedia.org/wiki/CNO_cycle

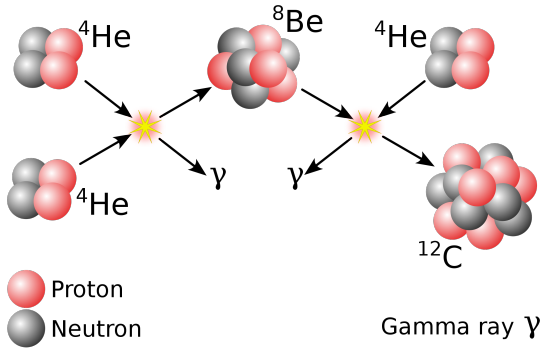

Figure 1.5: Schematic view of the triple-alpha process, showing the formation of ^{12}C by helium fusion (credit: *Wikipedia*[3]).

$$\begin{cases} {}^4\mathrm{He} + {}^4\mathrm{He} \rightleftharpoons {}^8\mathrm{Be} + \gamma \\ {}^4\mathrm{He} + {}^8\mathrm{Be} \rightarrow {}^{12}\mathrm{C} + \gamma \end{cases} \tag{1.4}$$

1.2.2 The AGB phase

After the exhaustion of the core helium, the stellar core will start to contract again, as it did at the end of the MS phase. For stars with birth masses ($M_\star$) $\lesssim 8\ M_\odot$, this will result in the formation of a degenerate core composed mainly of carbon and oxygen. These stars are not massive enough to attain core temperatures high enough to fuse carbon. They now pass through the *asymptotic giant branch* (AGB) phase, characterised by an inert C-O core, and burn helium and hydrogen in successive shells outside the core. The evolution along the AGB can be divided into two distinct stages, the *early* AGB (E-AGB) and the *thermally-pulsing* AGB (TP-AGB).

1.2.2.1 Early AGB

In this phase, the star has just begun its ascent along the AGB. The energy production in the star at this stage is initially dominated by the shell burning of He above the core. However, the luminosity of the star keeps increasing due

[3] https://en.wikipedia.org/wiki/Triple-alpha_process

to the larger and larger energy being output by the shell-H burning in a region further outside than the He-burning shell (see Sect. 2.3.2). After around 10^5 years, the luminosity of the star will come to be dominated by the H-shell. For stars in the mass range 4 - 8 $M_\odot$, the second dredge-up (see Sect. 2.3.2.3) occurs during this period, and results in the enriching of the stellar surface with products from the CNO cycle. The E-AGB stage is understood to last for approximately 10^6 to 10^7 years (Vassiliadis & Wood 1993).

1.2.2.2 Thermally-pulsing AGB

During the shell burning of He and H, the energy production from the He shell will increase to very high (10^6 to 10^7 $L_\odot$) values over a relatively short timescale of around 100 years. This happens due to explosive thermonuclear runaway in the triple-alpha process in the He-shell owing to the continuous accumulation of helium on it from the H-shell burning above. This process is termed the *helium shell flash*. It brings about convectional instabilities in the stellar envelope, and leads to the third dredge-up (TDU, see Sect. 2.3.2.3). These processes together, i.e., the helium shell flash, the instabilities, and the subsequent TDU, are collectively called a *thermal pulse* (TP). AGB stars where thermal pulses occur are said to be in the TP-AGB phase. TP events are repeated on a timescale ($\sim 10^3$-10^5 years) dependent on the stellar mass, as the quiescent He-shell burning is restarted by the repeated accumulation of helium from the H-burning shell. The number and intensity of these events depend on the birth mass and composition of the stars. The time between subsequent thermal pulses is termed the *interpulse* phase ($\sim 10^4$ years, Karakas & Lattanzio 2014). Fig. 1.6 shows the variation in the luminosities of the H and He burning shells, and the total radiated surface luminosity in the TP-AGB phase (Karakas & Lattanzio 2014).

During the AGB phase, several interesting and complex phenomena take place, including processes like hot bottom burning (see Sect. 2.3.2.4), and strong mass loss (Sect. 2.4) which creates chemically-rich circumstellar envelopes (CSEs, Sect. 2.5). The structure, evolution, and properties of AGB stars are explored in more detail in Chapter 2. The remaining chapters of this thesis will focus exclusively on AGB stars.

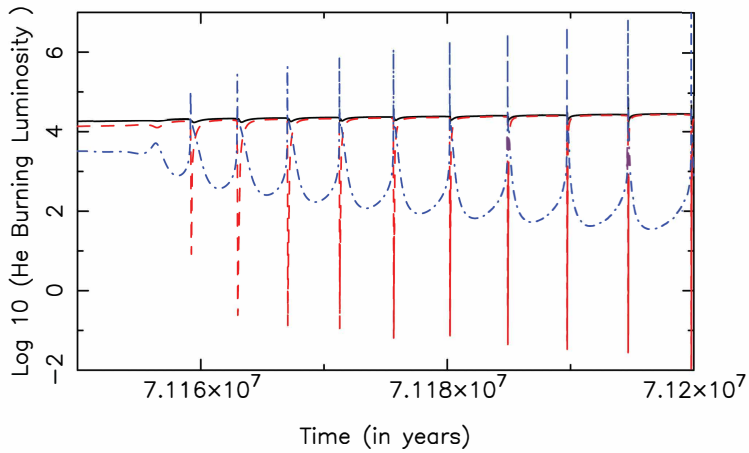

Figure 1.6: Variation in luminosity from the H (blue) and He (red) burning shells, and the total radiated surface luminosity (black) during the TP-AGB phase (credit: Karakas & Lattanzio 2014).

1.2.3 Post-AGB evolution

At the end of the AGB phase, the convective envelope decreases in mass, and the thermal pulses (Sect. 1.2.2.2) stop. The stars now move towards higher effective temperatures at roughly constant luminosity, and are known as post-AGB stars. The stellar and circumstellar envelopes are slowly ejected into the ISM, exposing the inert, luminous C-O core. In a timescale of around 10^4 years, the strong UV radiation from the central object will ionise the ejected material around it, forming objects known as planetary nebulae (PNe). The exposed core will eventually form a white dwarf (WD) star. The locations of the PN and WD stages in the HR diagram are shown in Fig. 1.2. Over the course of billions of years, the WD object will cool down and become invisible as a black dwarf.

1.3 The evolution of massive stars

Massive stars ($M_\star$ > 8-10 $M_\odot$) are known as known as supergiants or hypergiants, due to their very high luminosities (upto 10^6 $L_\odot$, see LeBlanc 2010).

These stars will evolve through the main sequence faster than low-mass stars. They then go on to fuse helium, and will continue to more cycles of nuclear burning in the core after the exhaustion of helium, forming heavier and heavier elements up to iron, and finally end their life in extremely bright *supernova* (SN) explosions, triggered by the sudden implosion of their cores. During a supernova explosion, the outer layers of the star may be violently ejected into the interstellar medium. The core remnant that remains after the explosion may form a neutron star or a black hole, depending on the mass of the star. The details of these processes will not be discussed here, as the central focus of this work is the AGB. The reader is referred to Kippenhahn & Weigert (1990) or LeBlanc (2010) for an elaborate discussion on the evolution and end stages of such massive stars.

2

AGB stars and why to study them

The contents of this chapter are broadly based on Habing & Olofsson (2003) and Herwig (2005), which serve as the general reference wherever other literature is not explicitly cited.

2.1 Introduction

The brightest stars in galaxies are often on the AGB, with luminosities rising up to as much as 10^4 times the solar value. However, AGB stars are also very cool objects, with surface temperatures around just 2000-3000 K. This is due to the fact that their radii are very large, with the stellar surface extending up to several 100 times the solar radius. The low surface temperatures also mean that they are very faint and dust-obscured in the optical, and are invisible to the naked eye, but shine bright in the infrared. The stellar emission peaks at around 1μm, making these stars appear very red.

The AGB is one of the most important phases in the stellar lifecycle. It is the last stage in which the star can release nuclear energy. The evolution to and from the AGB was briefly described in Section 1.2. This chapter focuses on the physical properties of AGB stars and their circumstellar envelopes, and

paves the way for a more elaborate discussion of circumstellar chemistry in Chapter 4.

2.2 Classification of AGB stars

AGB stars are classified mainly on the basis of their atmospheric carbon-oxygen elemental abundance ratio (C/O). This scheme splits AGB stars into three categories or chemical types: *(1)* M-type stars, or oxygen-rich stars (C/O<1), *(2)* C-type stars or carbon-rich stars (or simply carbon stars, C/O>1), and *(3)* S-type, or intermediate stars (C/O$\lessapprox$1). This categorisation is very useful in investigating the variations in circumstellar chemistry across AGB CSEs (see Chapter 4).

At the start of the AGB, typical C/O ratios found in stars are around 0.3. As the star evolves, the C/O ratio changes. Newly nucleosynthesised ^{12}C is brought to the surface by dredge-ups (see Sect. 2.3.2.3), increasing the C/O ratio. For stars with $M_\star > 4\ M_\odot$, the effect of this process is decreased, as some ^{12}C is removed from the surface by hot bottom burning (HBB, see Sect. 2.3.2.4), by reprocessing the ^{12}C in the CNO cycle.

In addition to the spectral-type classification, AGB stars are also classified on the basis of their variability (see Sect. 2.3.3.1), into three main groups: *(1)* Mira variables, *(2)* Semi-regular (SR) variables, and *(3)* Irregular variables. Miras are typically well-evolved AGB stars having regular periods and showcasing large amplitudes. The semi-regular variables have smaller amplitudes, and are further divided into two subgroups, SR type-a (SRa), which are still mostly regular, and SR type-b (SRb), with poor regularity. The irregular variables present ill-defined periods at very small amplitudes. Fig. 2.1 shows the V-band light curves of a Mira variable and a semi-regular variable star.

2.3 The structure of AGB stars

The structure of an AGB star can be divided into four major components: *(1)* the core, *(2)* the stellar envelope *(3)* the stellar atmosphere, and *(4)* the circumstellar envelope (CSE). The physical and chemical processes taking place in these regions are schematically shown in Fig. 2.2. The temperature and density fall drastically as we move to the successive outer layers from the stellar core. The characteristics of these four components are described below.

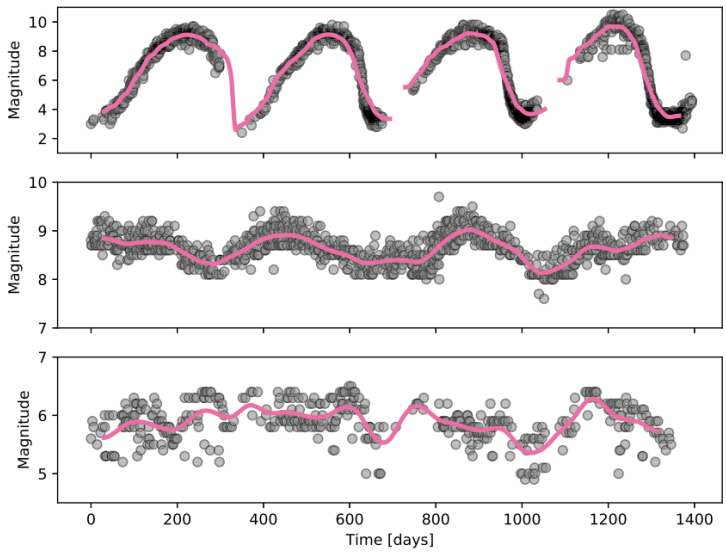

Figure 2.1: V-band light curves of the Mira variable o Ceti (top), and the semi-regular variables RU Cyg (SRa, middle) and R Dor (SRb, bottom), (credit: Liljegren 2018).

2.3.1 The core

The core is the central, innermost region of an AGB star, having only 0.5−1 $M_\odot$ in mass, and extending only to less than 0.01% of the total radial size of the star. The core is the hottest and densest part of the star, with temperatures of up to 10^8 K, and densities already comparable to that of white dwarfs. In contrast to the core of a main sequence star, the AGB core is inert and does not carry out nuclear fusion. It is composed mainly of carbon, oxygen, and degenerate electrons, and is often called an inert C-O core. The composition and properties of the core do not change significantly during the AGB phase, owing to its degeneracy, implying that unlike in the previous evolutionary phases, AGB evolution is no longer controlled exclusively by the evolution of the core (see Sect. 2.4).

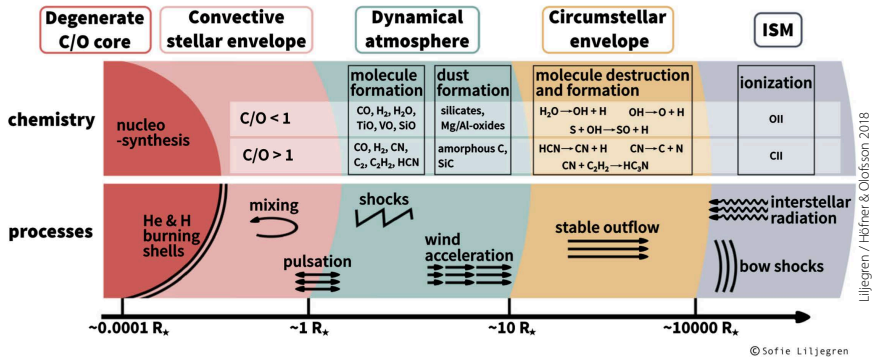

Figure 2.2: A schematic view (not to scale) of the inner layers, atmosphere, and the circumstellar envelope of an AGB star (credit: Höfner & Olofsson 2018).

2.3.2 The stellar envelope

The stellar envelope is the large, hot region surrounding the core, and it contains roughly 50−80% of the stellar mass. Around 99.99% of the size of the star is constituted by the envelope. Fig. 2.3 shows a schematic diagram of the core and envelope structure of an AGB star. The stellar envelope consists of two shells of alternate nuclear burning, an inner one of helium, and an outer one of hydrogen. These shells are separated by an intershell region (Fig. 2.3). The majority of the stellar envelope is comprised of a large convective envelope, lying above the hydrogen-burning shell, and reaching up to the surface of the star. For stars of low envelope masses, a thin radiative shell lies between the H-burning shell and the convective envelope.

2.3.2.1 Nucleosynthesis: fusion

The primary nucleosynthesis in AGB stars occurs in the two shell regions described above. In the outer shell, H is fused to form ^{4}He, principally via the CNO cycle. This influences the composition of the intershell region below it, which is processed by the inner He-burning shell. There, He is burnt via the triple-alpha process to form ^{12}C. See Karakas & Lattanzio (2014) for an elaborate review of the nucleosynthesis and stellar yields of AGB stars.

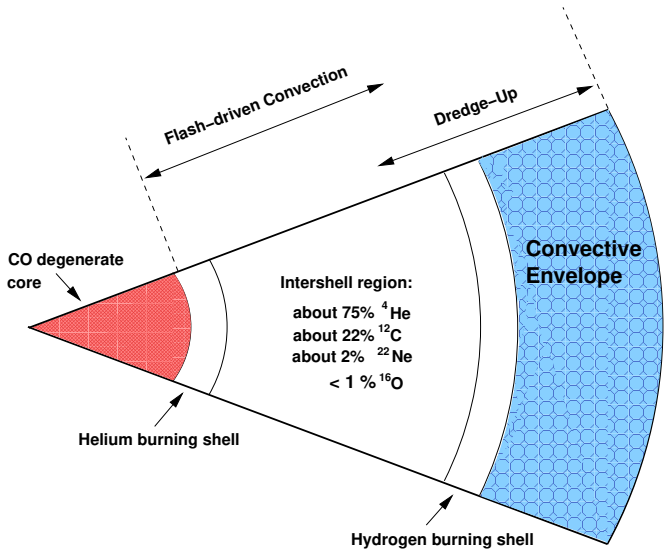

Figure 2.3: Schematic view of the core and stellar envelope of an AGB star (credit: Karakas & Lugaro 2010).

2.3.2.2 Heavy element nucleosynthesis: the s-process

The slow neutron-capture process or simply the s-process involves, as the name suggests, slow capture of neutrons followed by β^- decay, leading to the formation of successively heavier elements. The s-process elements, like lead, technetium and zirconium, are produced in the helium-rich intershell region (Fig. 2.3) between the H and He burning shells. Fig. 2.4 shows an example of s-process nucleosynthetic pathways. During the dredge-ups (see Sect. 2.3.2.3), the s-process elements are brought from the intershell region to the surface of the star, where they are incorporated into the stellar wind, eventually enriching the ISM.

2.3.2.3 Dredge-ups

During the evolution of a star, there are multiple *dredge-up* processes that bring up the nuclear-burning products from the interior of the star to the surface (Iben 1975; Sugimoto & Nomoto 1975). The first dredge-up (FDU) occurs during the red-giant branch (RGB, see Sect. 1.2.1.2), when the convec-

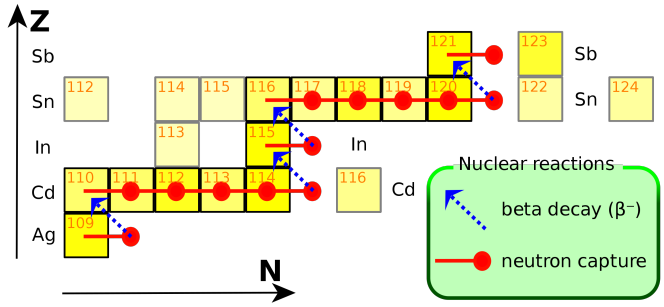

Figure 2.4: Example of a typical s-process nucleosynthesis sequence, from Ag to Sb (credit: *Wikipedia*[1]).

tive envelope penetrates inwards, mixing the products from partial H-burning to the surface. This decreases the surface abundance of ^{12}C, while increasing those of ^{13}C and ^{14}N.

The second dredge-up (SDU) occurs in stars heavier than 4 $M_\odot$, during the early AGB (E-AGB, see Sect. 1.2.2.1) phase, after the exhaustion of core helium burning. This time, the convective envelope brings up material from the old burning layers, which are rich in He and ^{14}N, to the surface layers of the young AGB star. Owing to the increased luminosity following the helium shell flash (see Sect. 1.2.2.2), a third dredge-up (TDU) occurs, due to the convective envelope penetrating what was previously the intershell convection zone. He and ^{12}C are mixed upwards int this process. Repeated TDU events significantly alter the stellar surface abundances of AGB stars, increasing, in particular, the amount of ^{12}C at the surface. Fig. 2.5 shows the time evolution of C/O and ^{12}C/^{13}C ratios during the AGB, for stars of masses 4, 5, and 6 $M_\odot$.

2.3.2.4 Hot bottom burning (HBB)

In thermally-pulsing AGB (TP-AGB, see Sect. 1.2.2) stars with masses above $\sim$5 $M_\odot$ (at solar metallicity, Siess et al. 2002), the thin radiative layer present between the hydrogen-burning shell and the convective envelope can disappear if the bottom of the convective envelope reaches temperatures ($3-8\times10^7$K) high enough to start nuclear burning. Such a situation is called *hot bottom*

[1] https://en.wikipedia.org/wiki/S-process

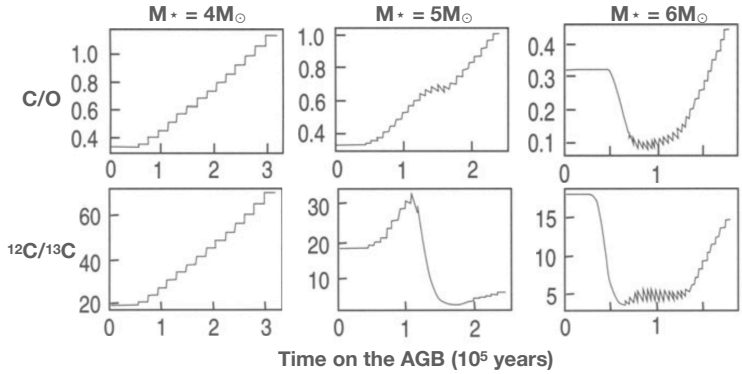

Figure 2.5: Time evolution of C/O and $^{12}C/^{13}C$ ratios during the AGB, for stars of masses 4 (left), 5 (center), and 6 $M_\odot$ (right). Credit: Lattanzio & Wood, in Habing & Olofsson (2003).

burning (HBB, Iben 1973; Sackmann et al. 1974). The CNO cycle products produced by HBB are immediately transported via convection to the surface of the star, leading to an increase in the surface abundance of ^{13}C and ^{14}N, at the cost of a reduced abundance of ^{12}C, counteracting the effect of the third dredge-up (see Sect. 2.3.2.3).

2.3.3 The stellar atmosphere

The name *atmosphere* is attributed to the layers immediately above the convective envelope of the AGB star. It is the outermost layer of the star, often viewed as the *surface* of the star, and is the region where the stellar wind originates. The interplay of various complex physical phenomena in the stellar atmosphere is crucial to mass loss and AGB evolution.

2.3.3.1 Pulsations

Radial pulsations arise in the outer parts of the convective envelope of AGB stars due to opacity effects (e.g. Bowen 1988). These intrinsic pulsations lead to repeated contractions and expansions of the photosphere, leading to periodic variations in the stellar brightness and radius. AGB stars are long-period variables (LPVs) with pulsation periods ranging from 10 to around 2000

days. Pulsations produce supersonic shock waves that propagate through the atmosphere of the star, heating up, compressing, and pushing out material (e.g. Cherchneff 2006; Liljegren 2018). This process plays an important role in driving the stellar wind (see Sect. 2.4).

2.3.3.2 The formation of molecules

As the temperatures of the atmospheric layers of AGB stars are ∼3000 - 4000 K, they are cool enough to allow the formation of molecules. For carbon-rich (C-type) stars, the main molecules formed are CO, HCN, CN, and C_2H_2, while oxygen-rich (M-type) stars form molecules including CO, H_2O, SiO, and SO_2 in their atmospheres. Convectional mixing and the presence of shocks caused by pulsations complicate the molecule formation process in the atmosphere. The broad emission and absorption bands of the formed molecules can be seen in the stellar spectrum of AGB stars, as shown in Fig. 2.6.

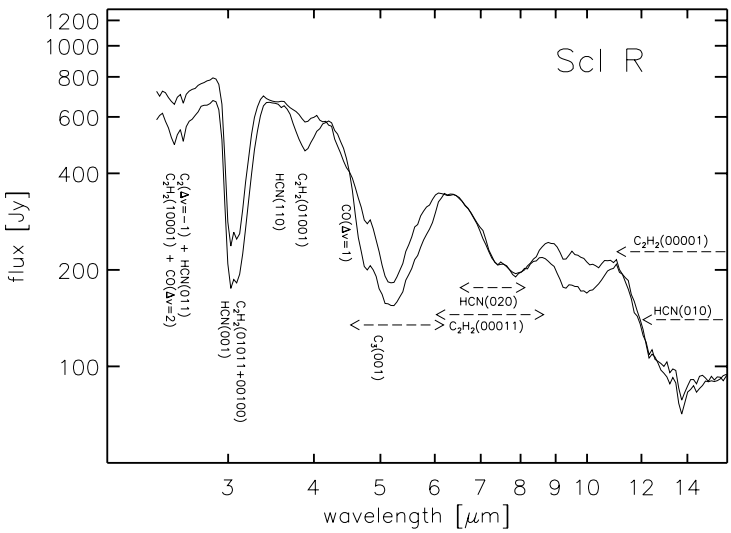

Figure 2.6: ISO-SWS spectra of the C-rich AGB star R Scl, at visual phases of 0.9 (thick) and 0.4 (thin). Quantum numbers of the upper vibrational levels are given in brackets after the molecule names (credit: Hron et al. 1998).

2.3.3.3 Dust

Along with the formation of molecules as described above, the cool and dense nature of the outer atmospheric layers of AGB stars also leads to the abundant formation of dust grains (e.g. Millar, in Habing & Olofsson 2003; Gail & Sedlmayr 2013; Höfner & Olofsson 2018). As discussed in Sect. 2.3.3.1, the density of the gas in the atmosphere is temporarily increased by pulsations which levitate its outer layers. This leads to an increase in the efficiency of the dust formation process. In C-stars, most of the dust is carbonaceous, composed mainly of amorphous carbon, whereas in the M-type stars, silicate dust is more predominant. See Gail & Sedlmayr (2013) for an in-depth study of dust formation and properties in AGB stars.

2.4 Dust-driven mass loss

AGB stars display heavy mass loss from the stellar surface into the surrounding ISM. The mass-loss rates of AGB stars are typically in the range of 10^{-8} to 10^{-4} $M_\odot$ yr^{-1}. The very high mass loss from the stellar surface outweighs the minor growth of the core that occurs as a consequence of the fusion processes ongoing in the shells. It is the mass loss that hence drives the onward evolution of AGB stars.

Outward motion of the top layers of the stellar atmosphere due to pulsations can not be the sole cause of the wind, as this process alone is not powerful enough to make these layers attain escape velocity (Wood 1979). The currently accepted formalism of the origin of AGB mass loss is the *dust-driven wind* model (e.g. Sedlmayr & Dominik 1995). In this scheme, dust formation occurs in the pulsation-levitated, shocked outer layers of the atmosphere. These dust grains are accelerated by the radiation pressure as they absorb and scatter photons from the central star. They then collide with and transfer momentum to the gas particles around them. Such dust-gas collisions create an outflow of gas and dust that we call the stellar wind.

The study of the causes and mechanisms of mass loss, and its dependence on fundamental stellar parameters, is crucial to understanding the evolution of AGB stars (e.g. Willson 2000). Numerical simulations like DARWIN (Dynamical Atmospheres and Radiation-driven Wind models with Implicit Numerics, Höfner et al. 2016) are being used extensively to study these phenomena further.

2.5 The circumstellar envelope

The circumstellar envelope (CSE) is the extended, tenuous, chemically rich environment surrounding the AGB star, formed by the extensive mass loss described above. The CSE can be divided into three regions, based on the variation in physical properties present within it. First, the *inner wind* is the region extending from the atmosphere to the dust-condensation zone. It presents exponentially falling gradients of temperature and density. Above it is the *intermediate wind* where dust forms and grows. The characteristics of this region are not yet well-understood. The part of the CSE from the radius where the wind has achieved terminal velocity, till it merges into the ISM is termed the *outer wind*. The density gradient in this region follows an r^{-2} distribution. CSEs are rich sites of molecule and dust formation, and complex chemistry. The various chemical processes and pathways taking place in AGB CSEs and some existing models are discussed in Chapter 4.

2.6 Building blocks of the universe

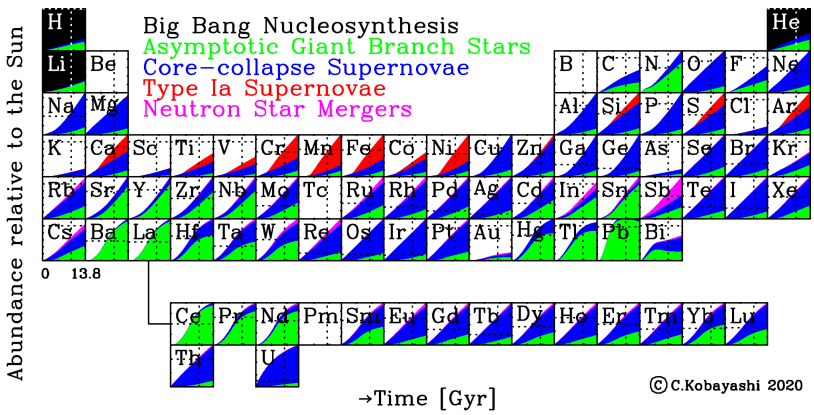

Figure 2.7: The periodic table of elements. Colours indicate different nucleosynthesis sources (credit: Kobayashi et al. 2020).

AGB stars play a major role in the universal cycle of matter, by nucleosynthesising heavy elements and releasing them into the ISM of their host

galaxies through their stellar winds. They are also responsible for the formation of dust grains. The periodic table of elements is shown in Fig. 2.7, with the different nucleosynthesis sources indicated by different colours. It can be seen that the AGB stars are major contributors of many elements, ranging from carbon and nitrogen, to the s-process elements like lead.

The mass loss from AGB stars thus forms the building blocks of the next generation of molecular clouds and stars (Tielens 2005). They are also drivers of the chemical evolution of galaxies. Therefore, a thorough characterisation of the physics and chemistry on the AGB is of paramount importance to astrophysics in general.

3

Molecules as diagnostic tools

The contents of this chapter are broadly based on Kwok (2007) and Wilson et al. (2013), which serve as the general reference wherever other literature is not explicitly cited.

Molecules, through their spectral lines, are excellent probes of the physical and chemical characteristics of circumstellar and interstellar gas. The intensity of a spectral line traces the amount and physical properties of the emitting matter, while the spectral line profile sheds light on its kinematics, and also reveals important details about optical depth effects. The line width, through Doppler broadening, is a direct measure of how fast the circumstellar material is moving.

The specifics of the molecular chemistry in the circumstellar envelopes of AGB stars will be dealt with in Chapter 4, and the major methods employed to observe line emission will be described in Chapter 5. This chapter offers a summary of the basic characteristics of molecular transitions and emission lines, examining how they are useful in estimating various properties of the emitting material.

3.1 Molecular transitions and line spectra

As is the case for atoms, molecules too have ground states and several excited states, and transitions between them. However, molecules are more complicated structures than atoms, and their Schrödinger equations are, therefore, more complex, and difficult to analyse directly. The *Born-Oppenheimer approximation* (Born & Oppenheimer 1927) offers some simplification, by stating that the nuclear and electronic motion in a molecule can be treated separately, dividing the molecular wave function into a nuclear and an electronic component. Energy levels of a molecule, and consequently the transitions between them, can then be divided into three separate categories, namely *electronic*, *vibrational*, and *rotational*, based on the type of energy level among which they occur. Fig. 3.1 shows a schematic of the arrangement of these three types of energy levels in a molecule. The classification of molecular transitions based on this division is briefly summarised below.

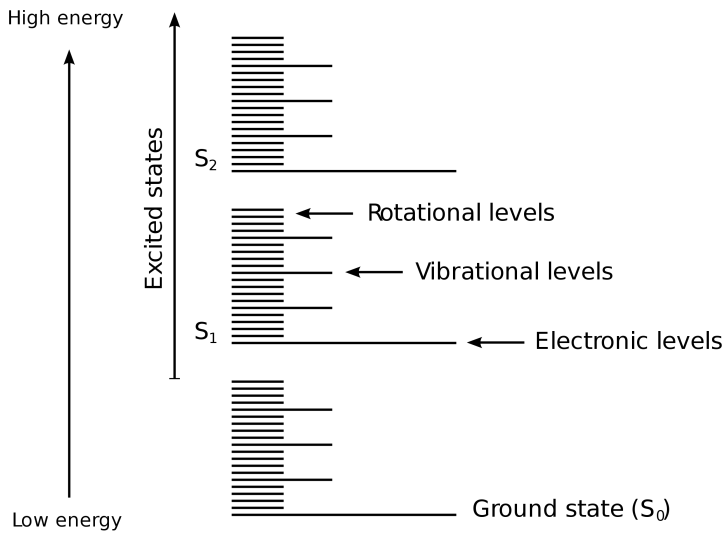

Figure 3.1: A schematic representation of the arrangement of the electronic, vibrational, and rotational energy levels of a molecule (credit: *Wikimedia Commons*[1]).

[1] https://commons.wikimedia.org/wiki/File:Molecular_energy_levels_en.svg

1. **Electronic transitions:** These are transitions caused by the excitation or de-excitation of electrons between the different electronic states or energy levels of the molecule. These energy levels are separated by large energy gaps ($\sim$ a few eV), and hence the spectral lines corresponding to these transitions fall in the visible or UV regions of the electromagnetic spectrum.

2. **Vibrational transitions:** These transitions arise from the oscillations or vibrations of the relative nuclear position with respect to its equilibrium position. There is a range of vibrational states within every electronic state. There can be different types of vibrations, depending on the type of molecule involved. For a diatomic molecule like CO, *stretching*, or the periodic elongation and compression of the bond between the constituent atoms forms the molecular vibration mode. For molecules with more than two atoms, stretching can be *symmetric* or *asymmetric*, and additional vibration modes, for e.g. *bending* (periodic change of the angle between bonds), and different combinations of the above, can also exist.
   For an N-atom molecule, there will be $3N$-5 vibration modes if it is linear, and $3N$-6 if non-linear. The typical differences between the energies of adjacent vibrational levels of molecules are in the range of 0.01-0.1 eV, and hence the corresponding spectral lines fall in the infrared part of the electromagnetic spectrum.

3. **Rotational transitions:** These transitions arise from the rotation of the nuclei, as a result of either the torque exerted by the irradiating field on the dipole of the molecule, or collisions. For molecules with no intrinsic dipole moment, like H_2 or C_2H_2, there can be no pure rotational transitions. Molecular rotational transitions have typical energies around $\sim 10^{-3}$ eV, leading to spectral lines in FIR, sub-mm and radio wavelengths. The CO $J = 1 - 0$ rotational transition at 115 GHz is a commonly studied example. It is also to be noted that rotational transitions are constrained by the electric dipole moment selection rule to have $\Delta J = \pm 1$ due to the symmetries in the rotational wave function of molecules.

In addition to the above, there are also *ro-vibrational* transitions, which involve changes in both the vibrational and rotational state of a molecule. The spectral lines of rotational transitions are what we observe using telescopes like ALMA and APEX (see Chapter. 5), and are the main tools employed in this work to study the physics and chemistry of circumstellar gas. As an example, Fig. 3.2 shows emission lines of SiO and HC_3N observed towards the AGB star IRAS 15194−5115 (Unnikrishnan et al. 2023). The molecules studied in this work, and the properties of the circumstellar material derived from the observed spectral lines will be discussed in Chapter 4. Sect. 4.2 of paper **??** explains in detail the methods employed to estimate molecular abundances from spectral lines, including *population diagrams* and analytical methods.

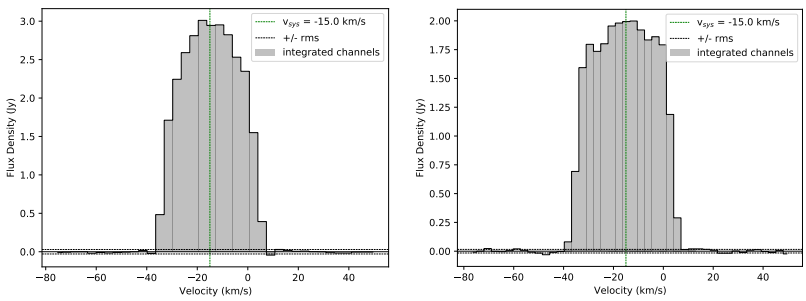

(a) SiO ($J = 2 - 1$) **(b)** HC_3N ($J = 11 - 10$)

Figure 3.2: Spectral lines of the SiO ($J = 2 - 1$, left) and HC_3N ($J = 11 - 10$, right) rotational transitions observed towards IRAS 15194−5115, using ALMA (credit: Unnikrishnan et al. 2023).

3.2 Hyperfine components

The energy levels of certain molecules are split into further divisions than those described above, due to the coupling of their spin- and orbital-angular momentum. This process is known as *spin-orbit coupling*, and leads to a splitting of the observed emission lines into components called *fine-structure*. In molecules like CN and C_2H, interactions between the electric or magnetic moments of the nuclei with electrons lead to further splitting of the energy

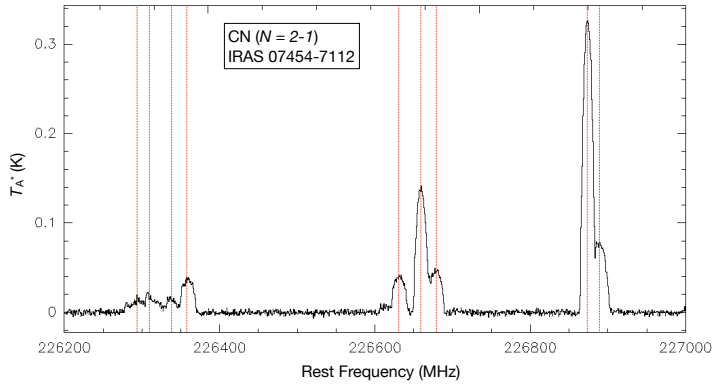

Figure 3.3: Hyperfine components of the CN ($N = 2 - 1$) rotational line towards the C-rich AGB star IRAS 07454−7112, observed with APEX. The red vertical lines denote the frequencies of the major components (credit: Unnikrishnan et al. (in prep.)).

levels, and consequently the line spectra, known as *hyperfine splitting*. Fig. 3.3 shows the hyperfine components in the line spectrum of the CN ($N = 2 - 1$) rotational line towards the C-rich AGB star IRAS 07454−7112.

3.3 What can molecules tell us?

Molecular spectra can be analysed to reveal a host of information about the astrophysical environments from which the emission originates. Different molecules, depending on their characteristics, are used to trace different properties of the sources. In AGB CSEs, the emission from carbon monoxide (CO) is often used to derive the major physical properties of the gas, such as its mass, temperature, density, and velocity. The observed profiles of these quantities form the basis of our models. H_2O, with its high dipole moment, serves as a good tracer of the variations in the radiation field throughout the CSE. Using high spectral-resolution observations, the kinematics and dynamics of the stellar winds, including expansion velocities, asymmetries, and turbulence, can be studied in great detail.

The excitation analysis, abundance calculations, and mapping of the emission from other molecules, such as SiO, HCN, and HC_3N, are used to further

constrain the physical properties of CSEs, and also to study the chemistry of the gas, as described in Chapter 4. The more molecules we can detect, study, and compare, the more we can say about the chemical processes and pathways occurring in circumstellar environments. Observations of different isotopologues of molecules can help constrain the isotopic ratios of various elements, like $^{12}C/^{13}C$, which can be used to study the evolutionary history of the star. For example, the three stars studied in paper **??** have very different $^{12}C/^{13}C$ ratios. We derived the isotopic ratios of carbon, silicon, and sulphur for the three stars. The estimates match well with the expected AGB values (see Table 8 of paper **??**).

3.4 Spectral surveys: how and why

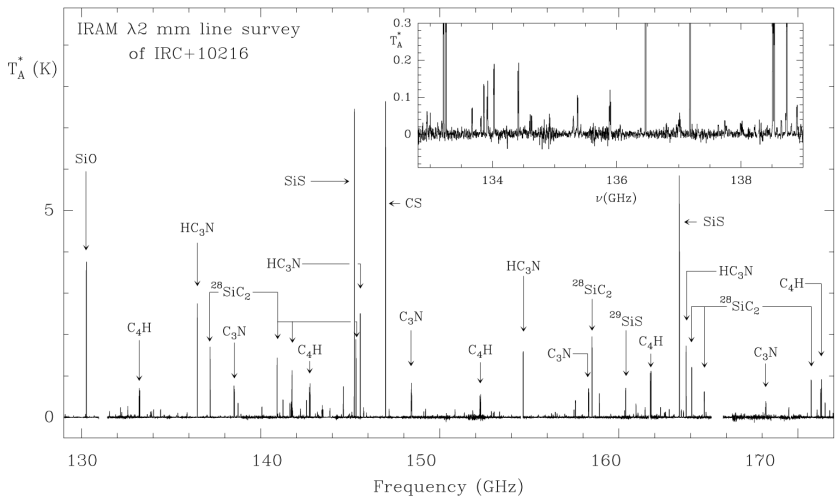

Figure 3.4: The IRAM 30-m spectral survey of the C-rich AGB star IRC +10 216, showing the identified lines (credit: Cernicharo et al. 2000).

Targeted observations of specific spectral lines, for e.g. those of CO, are used to study specific properties of AGB CSEs, as mentioned in Sect. 3.3. In addition, a vast amount of information about the chemistry of these outflows can be obtained by observing their spectra across wide bandwidths, not tar-

geted specifically at any molecule, but to obtain as many emission lines from various molecules as possible. This type of observation is commonly known as an *unbiased spectral survey*, as it is not biased to any particular molecular species. This is the mode of observation employed in this work.

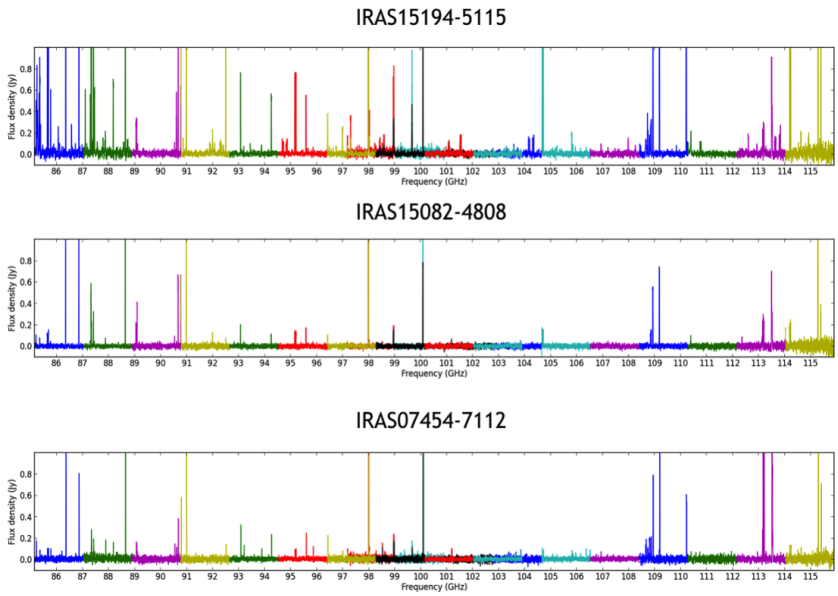

Figure 3.5: Overview of the spectral survey of three C-rich AGB stars, IRAS 15194−5115 (top), IRAS 15082−4808 (middle), and IRAS 07454−7112 (bottom). Colours indicates spectral windows of ALMA observations (adapted from Unnikrishnan et al. 2023).

Such spectral surveys have led to the detection of many new molecules. For example, around half of the total molecules detected to date towards the nearby carbon-star IRC +10 216 were discovered in the course of such a survey of that star by Cernicharo et al. (2000), using the IRAM 30-m telescope. An overview of this survey, showing the large number of detected molecules, is shown in Fig. 3.4. The ALMA band 3 spectral surveys performed in this work, towards three C-rich AGB stars, IRAS 15194−5115, IRAS 15082−4808, and IRAS 07454−7112, are shown in Fig. 3.5.

4

Circumstellar chemistry

As discussed in Chapter 2, AGB stars are highly complex, evolved objects which play a major role in the cosmic chemical cycle. They present extensive mass loss, and their circumstellar envelopes are interesting chemical factories, harbouring numerous molecules and dust species produced through a variety of chemical pathways. This chapter highlights some models and observational results, and the different factors and processes involved therein.

4.1 Molecules around AGB stars

Molecule formation from atomic matter in AGB stars starts in the warm ($\sim$3000 K), high-density, outer layers of their atmospheres (Sect. 2.3.3.2). To date, 107 molecular species, and their different isotopologues, have been detected in circumstellar environments (Table 4.1), ranging from two-atom molecules like CO and SiO, to relatively long carbon chains like C_8H, and large cyanopolyynes like HC_7N and $HC_{11}N$. Salts like NaCl and KCl, and refractory heavy metal oxides including AlO and TiO_2 have been detected in AGB CSEs. These species and their spectral lines can be used to estimate various characteristics of circumstellar matter, as described in Chapter 3.

Table 4.1: Molecules detected in circumstellar envelopes, sorted left to right in the increasing order of the number of constituent atoms, indicated at the top of each column. Source: the CDMS catalogue (Müller et al. 2005), and McGuire (2022). See McGuire (2022) for the references to the publications presenting the detection of each of the below species.

2	3	4	5	6	7	≥8
AlF	C_3	l-C_3H	C_5	C_5H	C_6H	C_7H
AlCl	C_2H	C_3N	C_4H	l-C_4H_2	CH_2CHCN	C_6H_2
C_2	C_2S	C_3O	C_4Si	C_2H_4	CH_3C_2H	CH_3SiH_3
CN	HCN	C_3S	c-C_3H_2	CH_3CN	HC_5N	MgC_6H
CO	HCO^+	C_2H_2	CH_4	C_5N	C_6H^-	HC_7N
CP	H_2O	NH_3	HC_3N	l-HC_4N	MgC_5N	C_8H
SiC	H_2S	H_2CO	HC_2NC	C_5N^-		C_8H^-
HCl	HNC	H_2CN	HNC_3	MgC_4H		HC_9N
KCl	MgCN	H_2CS	SiH_4	C_5S		$HC_{11}N$
NaCl	MgNC	SiC_3	CH_4^-	HC_4H		C_6H_6
OH	NaCN	C_3N^-	C_4H^-	SiH_3CN		
PN	SO_2	PH_3	MgC_3N			
SO	SiC_2	HC_2N	SiC_4			
SiN	CO_2	HMgNC				
SiO	AlNC	MgCCH				
SiS	SiNC					
CS	HCP					
CN^-	SiCN					
SiP	SiNC					
PO	C_2P					
AlO	KCN					
TiO	FeCN					
VO	C_2N					
	KCN					
	Si_2C					
	CaNC					
	MgC_2					
	AlOH					
	TiO_2					

In the work presented in paper **??**, we identified a total of 311 emission features belonging to 49 molecules (including isotopologues, see Table A.1 of paper **??**) in the ALMA band 3 survey of three C-rich AGB CSEs (see Sect. 3.1 of paper **??**).

4.2 Diversity among AGB CSEs

Among the different categories (M-S-C, see Sect. 2.2) of AGB stars, the carbon-rich (C-type) stars are the richest in terms of the number and diversity of molecules formed. While the CSEs of M-type stars present relatively small molecules including CO, H_2O, etc., and a few larger molecules like NH_3, the detection of larger molecules like long-chain hydrocarbons (C_nH) and cyanopolyynes (HC_nN) have been done only towards C-type CSEs. Most of these detections have been made towards the nearby, extreme C-rich AGB star IRC +10 216, which is the most studied AGB star to date (see Sect. 4.4.1).

A similar difference can also be seen in the dust species present in M-type and C-type CSEs (e.g. Gail & Sedlmayr 2013; Höfner & Olofsson 2018). In the CSEs of M-type stars, the dominant dust species are silicates. Based on 9.7- and 18-μm solid-state features, several amorphous silicates have been identified in these stars (see Dorschner 2010, and references therein). Further, alumina (Al_2O_3) and crystalline silicate dust have also been detected towards some M-type stars (e.g. Blommaert et al. 2006, 2014). A detailed modelling of the dust formation in oxygen-rich CSEs was presented by Gobrecht et al. (2016). In contrast, the CSEs of C-type stars are dominated by amorphous carbonaceous dust (e.g. Kraemer et al. 2019; Sloan et al. 1998; Zijlstra et al. 2006), and also show features ($\sim$11.3 μm) of SiC (e.g. Ventura et al. 2014). The nature and types of dust formed in AGB stars are thus dependent on the stellar C/O ratio, which is influenced by the evolutionary pathway of the star, as in the occurrence or not of processes like hot bottom burning. Other factors, including metallicity, also play important roles in the formation of dust in AGB stars (e.g. Tosi et al. 2022).

4.3 Chemical stratification

The radial division of AGB CSEs into the inner-, intermediate-, and outer-wind regions was discussed in Sect. 2.5. Fig. 4.1 shows a schematic diagram of

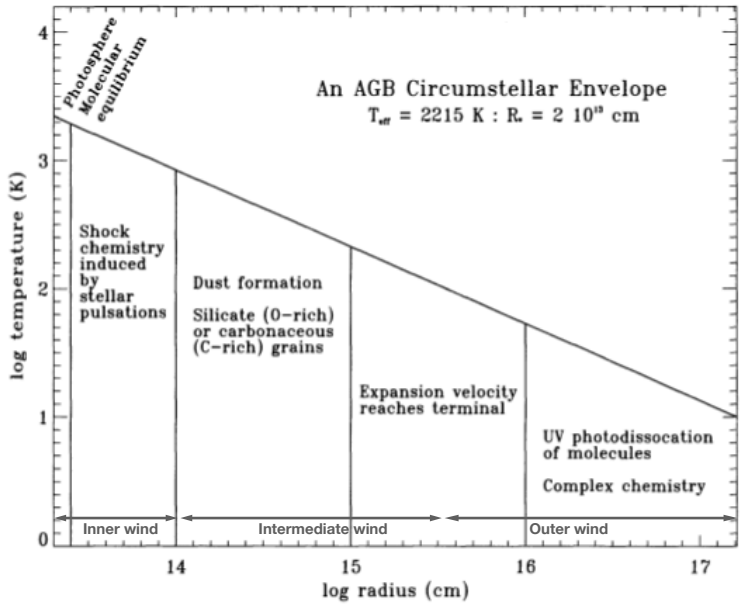

Figure 4.1: Schematic diagram of the chemical structure of an AGB CSE. (adapted from Markwick 2000).

the chemical structure of an AGB CSE, outlining the physical and chemical processes taking place in these regions. The molecules formed in the outer layers of the stellar atmosphere are transported outwards in the stellar wind, and involve in various chemical reactions in the CSE, particularly in the outer wind, which is the site of most of the complex chemistry in these sources. The outer wind is characterised by cool gas, expanding at terminal velocity. The molecules in these low-density outermost regions of the CSE are subject to photodissociation by the UV radiation from the interstellar radiation field (ISRF), giving rise to the formation of a multitude of interesting species.

Based on their position in this formation-destruction-formation pathway of circumstellar species, the molecules in AGB CSEs can be categorised into two groups, namely *parent* molecules and *daughter* molecules, as described below.

- **Parent molecules:** These are species which are formed from atomic gas

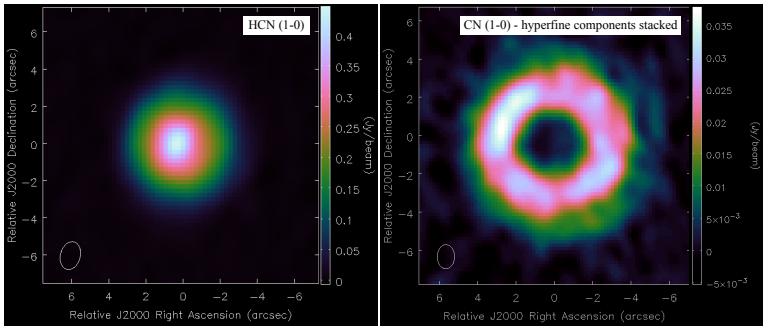

Figure 4.2: Systemic-velocity maps of the $J = 1-0$ line emission of HCN (left) and CN (right), showing centrally-peaked and shell emission respectively (credit: Unnikrishnan et al. 2023).

in the inner wind. These include mainly C_2H_2, HCN, CH_4, H_2S, NH_3, CO, CS, SiO, SiS, and N_2 (e.g. Cordiner & Millar 2009; Agúndez et al. 2012). The brightness maps of the line emission from parent molecules present *centrally-peaked* morphologies, i.e., emission that peaks close to the central star (in the inner wind) and extends radially outwards (see Sect. 4.1 of paper **??**).

- **Daughter molecules:** These are species which are formed from the parent molecules, through photodissociation or other chemical pathways. They are found in the outer wind. Most of the species detected in CSEs, including long-chain hydrocarbons and cyanopolyynes are daughter species formed in the CSE from their parent progenitors. These species are distributed in hollow spherical *shells* in the outer CSE, as indicated by their line emission maps which show no emission near the central star, but peak in shells radially farther away (see Sect. 4.1 of paper **??**).

The *centrally-peaked* HCN, and the *shell* CN emission morphologies for the carbon star IRAS 07454−7112 mapped by ALMA are shown in Fig. 4.2. This is consistent with the fact that CN is a photodissociation product of the parent species HCN. The nature of photodissociation of the constituent molecules, i.e., whether they are dissociated in lines or the continuum, and their shielding

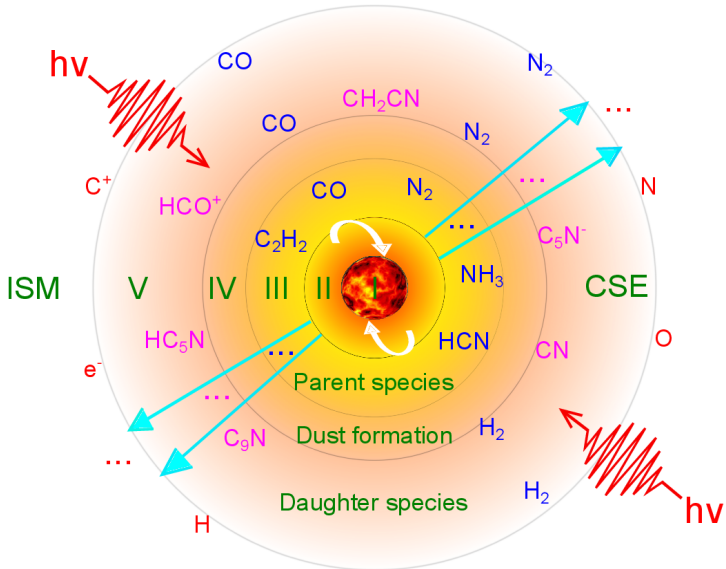

Figure 4.3: Schematic of the chemistry in a circumstellar envelope, showing parent and daughter species. The regions marked in Roman numbers are: (I) degenerate C-O core and He, H burning shells, (II) convective atmosphere, (III) shocked inner wind where parent species are formed, (IV) intermediate wind, (V) outer wind where daughter species are formed primarily by photodissociation, (VI) the ISM. (credit: Li et al. 2014).

efficiencies, have significant influence on the gas-phase chemistry in the CSE. In particular, the photodissociation of CO (e.g. Saberi et al. 2019) is key in precisely determining the extent of circumstellar outflows and their mass-loss rates.

Fig. 4.3 shows an overview of the radial variation in chemistry for a typical CSE, schematically depicting the radial arrangement of parent and daughter species. The various chemical pathways in AGB CSEs are subject to intensive study, both through observations and chemical modelling. With the development of modern interferometers like ALMA, VLA, and NOEMA, it is now possible to resolve and map the circumstellar envelopes of AGB stars, and study the chemical structure of these sources in detail (e.g. Dinh-V-Trung & Lim 2008; Velilla Prieto et al. 2015; Maercker et al. 2016; Agúndez et al. 2017; Unnikrishnan et al. 2023). Single-dish spectral surveys have also sig-

nificantly advanced our knowledge of circumstellar molecules (e.g. Cernicharo et al. 2000; De Beck et al. 2012; De Beck & Olofsson 2018, 2020; Velilla Prieto et al. 2017). Such observational studies, along with the advances in our knowledge of chemical reaction networks and rates, have led to the development of detailed chemical models fine-tuned for AGB circumstellar environments (e.g. Brown & Millar 2003; Cordiner & Millar 2009; Agúndez et al. 2017; Van de Sande et al. 2019, 2020, 2021).

Radiative transfer modelling is also a regularly employed tool to obtain rigorous estimates of molecular abundance profiles from observations. Agúndez et al. (2012) constrained the abundances of molecules formed in the inner layers of the CSE of IRC +10 216 using radiative transfer calculations on observations with the IRAM 30-m telescope. De Beck et al. (2012) presented similar models for CO and C_2H towards IRC +10 216, based on IRAM 30-m and Herschel/HIFI observations. The abundance profiles of sulphur-bearing species in the CSEs of M-type AGB stars were studied using radiative transfer models by Danilovich et al. (2016, 2019, 2020). We note that this is not a comprehensive overview.

4.4 Carbon chemistry

The circumstellar envelopes of carbon-rich AGB stars present a larger number of molecules and more complex chemistry compared to those of oxygen-rich (M-type) AGB stars. This is primarily due to the larger versatility of the carbon atom compared to that of oxygen in terms of possible chemical reactions and pathways, due to its higher valency. The increased ability of carbon to form stable long-chain molecules (catenation), owing to the high bond-strength between C-atoms, also leads to the presence of large, complex molecules in C-rich CSEs. The high carbon abundance also allows the formation of a large number of carbon-bearing species, possibly including polycyclic aromatic hydrocarbons (PAHs, e.g. Cherchneff et al. 1992; Allain et al. 1997), which are not found in M-type CSEs.

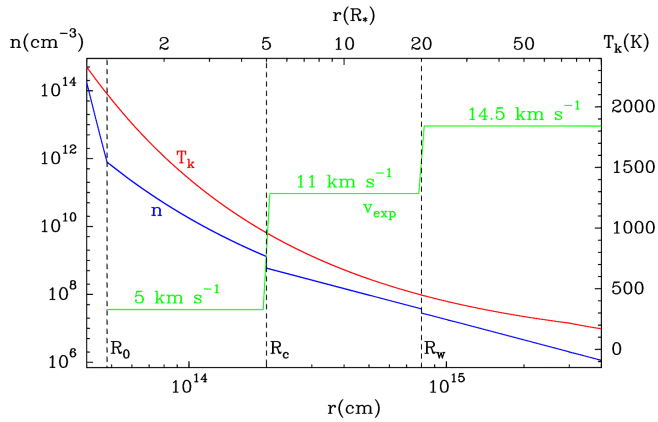

Figure 4.4: Model of the number density (n), temperature (T_k), and velocity (v_exp) profiles of IRC +10 216. R_0, R_C, and R_W correspond to the radius of the static atmosphere, dust condensation radius, and the end of the dust acceleration region, respectively. (credit: Agúndez et al. 2012).

4.4.1 The story so far: IRC +10 216

IRC +10 216, also known as CW Leonis, is a nearby (120-190 pc, Groenewegen et al. 2012; Andriantsaralaza et al. 2022), carbon-rich (C/O $> 1.5 \pm 0.4$, Fonfría et al. 2022) AGB star, with a high mass-loss rate ($\dot{M}$=2-4×10^{-5} $M_\odot$ yr^{-1}, Guélin et al. 2018), making it an easy target for observations. Owing to these properties and the molecular richness in its CSE, the majority of the observational studies and chemical models of carbon-star CSEs so far have focussed on this object (e.g. Agúndez et al. 2017; He et al. 2008; Cernicharo et al. 2000; Cordiner & Millar 2009; Guélin et al. 2018; Pardo et al. 2022; Patel et al. 2011; Velilla Prieto et al. 2019; Van de Sande et al. 2019). Hence, IRC +10 216 holds the status of an archetypal carbon-star. Fig. 4.4 shows a model of the radial number density, temperature, and velocity profiles of the CSE of the C-rich AGB star IRC +10 216, from Agúndez et al. (2012).

Line emission from molecular species in the CSE of IRC +10 216 has been analysed in detail in several studies. Agúndez et al. (2017) used ALMA to map the CSE of IRC +10 216 in various lines, including those of C_2H, C_4H, HC_3N, HC_5N, C_3N, and CN. Fig. 4.5 shows the systemic-velocity surface brightness maps of C_2H and CN towards IRC +10 216 from Agúndez et al.

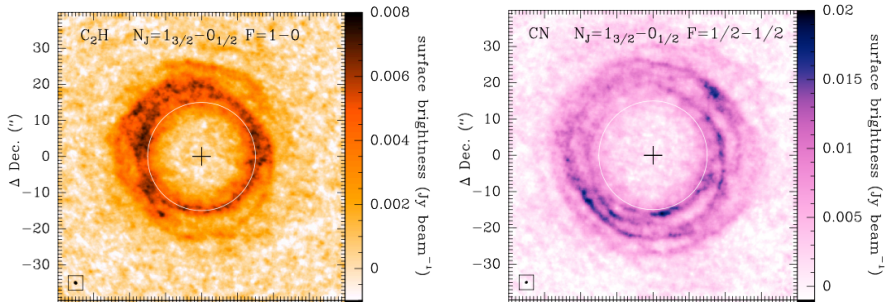

Figure 4.5: Systemic-velocity surface brightness maps of C_2H and CN towards IRC +10 216, observed using ALMA (credit: Agúndez et al. 2017).

(2017). From such maps, the radial surface brightness profiles of the species can be obtained, which can offer estimates of the sizes of the emitting regions of different molecules. These can help in obtaining accurate abundance estimates, and can also be used to fine-tune chemical models of C-rich CSEs, to gain a better understanding of the chemical reactions occurring in these environments. The observed and modelled radial surface brightness profiles of CN, C_3N, HC_3N, and HC_5N from Agúndez et al. (2017) are shown in Fig. 4.6.

The chemistry of silicon- and sulphur-bearing species in the CSE of IRC +10 216 has been explored by Velilla Prieto et al. (2015, 2019), and Massalkhi et al. (2019), among others. Patel et al. (2011) detected a large number of vibrationally-excited rotational lines arising from the inner envelope of IRC +10 216, in an interferometric spectral survey with the Submillimeter Array (SMA). Spectral surveys using Herschel have led to the detection of many lines from the high-energy rotational transitions of several molecular species including CO, HCN, CS, and SiC_2 (Cernicharo et al. 2010).

As seen in Fig. 4.5, the emission maps of different molecules trace distinct arc-like structures in addition to a broad shell. This is also seen towards the stars studied in this work (see Sect. 4.1.1. in paper **??**). These are indicative of large-scale radial density enhancements in the CSE, a deviation from the smooth, spherical CSE assumption. Recent chemical models have incorporated the existence of such density-enhanced shells, and hence offer more realistic predictions of the chemical abundances and emission profiles (e.g. Cordiner & Millar 2009). Van de Sande & Millar (2019) further extended

the relevant chemical models to include the effects of photo-induced chemistry and clumpiness in the CSE.

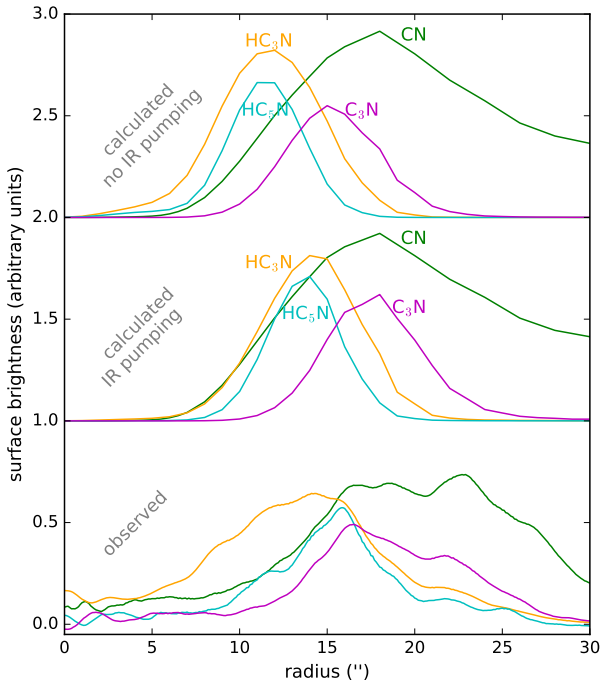

Figure 4.6: Modelled (top, middle) and observed (bottom) radial surface brightness profiles of CN, C_3N, HC_3N, and HC_5N towards IRC +10 216 (credit: Agúndez et al. 2017).

While there have been a large number of studies of carbon-star CSEs focussed on IRC +10 216 as discussed above, only a handful of studies have looked at other sources in detail. Around 20 carbon stars were detected in HCN (J=1-0) line emission by Olofsson et al. (1990). Bujarrabal et al. (1994) and Olofsson et al. (1998) observed samples of 16 and 22 carbon stars, respectively, in various molecular lines. IRAS 15194−5115 was observed in the 1.3 mm and 3 mm bands by Nyman et al. (1993) using the Swedish-ESO Submillimetre Telescope (SEST). Line emission from a sample of seven C-

rich AGB stars was surveyed in the mm/sub-mm wavelength range by Woods et al. (2003), using the Onsala 20 m telescope and the SEST, while similar studies were conducted using the Mopra 22 m telescope by Smith et al. (2015). Targeted, line-specific observations of larger source samples have also been performed by Schöier et al. (2013); Massalkhi et al. (2019) among others. Kim et al. (2015) interferometrically resolved the CO $J = 2 - 1$ emission from the CSE of the carbon star CIT 6, revealing a spiral shell pattern and a nascent bipolar outflow.

4.4.2 This work

The advent of high angular-resolution telescopes has enabled the mapping of AGB CSEs in previously unattainable detail and sensitivity. However, most of our current knowledge of the circumstellar chemistry of AGB stars, of the C-rich type in particular, is to date based on observations and models of IRC +10 216 alone, as discussed above. While the few studies of different carbon stars mentioned above indeed advanced our knowledge of the carbon chemistry in AGB CSEs, they were limited by the fact that most of them were single-dish observations, not intended to spatially resolve the circumstellar emission. Given that the accurate determination of molecular abundances requires knowledge of the sizes of the emitting regions, which are obtainable only by spatially resolving the emission, the lack of spatially-resolved observations of multiple C-rich CSEs limit our ability to compare and contrast the chemistry in these objects with one another, and put to test the chemical models optimised for IRC +10 216.

There have been no multi-source studies aimed at resolving the circumstellar emission from carbon-rich AGB CSEs other than IRC +10 216 so far, and this is where the need of the work described in paper **??** arises. The high-resolution ALMA observations of three C-rich AGB CSEs, IRAS 15194−5115, IRAS 15082−4808, and IRAS 07454−7112, presented in this work make it possible to obtain well-constrained estimates of the physical conditions and molecular abundances in these sources, enabling comparisons with one another and IRC +10 216. This can bring out similarities and differences in the chemical evolution of AGB CSEs, and also verify whether IRC +10 216 indeed is the archetype carbon star it is thought to be.

5

Observing techniques

5.1 Overview

The chemistry in AGB CSEs, described in Chapter 4, is best studied by observations of molecular emission lines. The spectral signatures of the rotational transitions (see Sect. 3.1) of molecular species fall in the *long-wavelength* regime, specifically in the far-infrared (∼15 - 200 μm), sub-millimeter, millimeter, and centimeter wavelengths. A major part of the continuum emission from circumstellar dust also falls in the mid-infrared (∼3 - 15 μm) to sub-mm wavelength range, whereas the stellar continuum from AGB stars peaks in the near-infrared (∼0.8 - 3 μm) wavelength range.

The available bandwidth for ground-based observations is severely limited by the Earth's atmosphere, as shown in Fig. 5.1. The amount of precipitable water vapour (PWV) present in the atmosphere affects its transparency. It is measured in millimeters, and is calculated based on combined radiometer measurements and atmospheric models of the telescope sites. PWV is strongly dependent on altitude and local weather. Fig. 5.2 shows the atmospheric transmission at the ALMA array operations site (AOS) at various PWV values.

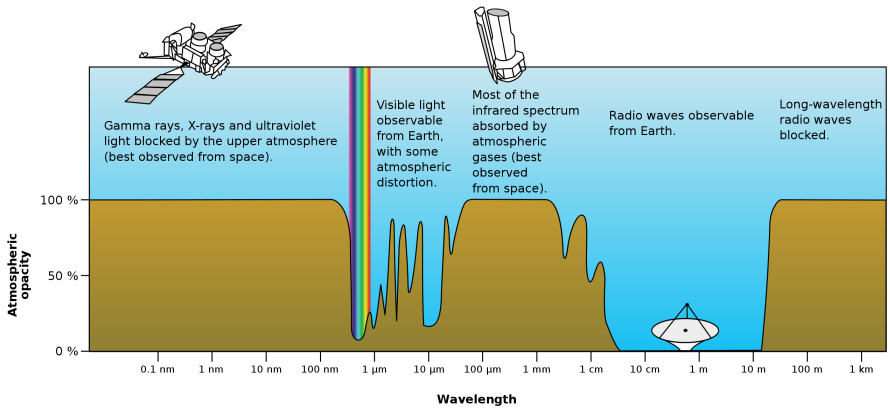

Figure 5.1: Opacity of the Earth's atmosphere across the electromagnetic spectrum (credit: NASA).

All of the radiation in the far-infrared is blocked from reaching the ground due to absorption by the water present in the Earth's atmosphere. To solve this problem, orbiting space telescopes like the Infrared Space Observatory (ISO) and later the Herschel Space Observatory were used to observe the FIR spectra of AGB stars, among other sources, from above the Earth's atmosphere. The recently launched James Webb Space Telescope (JWST) is also opening up possibilities of highly sensitive near- and mid-infrared astronomical observations from space.

In the sub-mm/mm regime, the presence of atmospheric water vapour poses a severe limitation to earth-based observations, and telescopes like the Atacama Pathfinder Experiment (APEX) and the Atacama Large Millimeter/submillimeter Array (ALMA) have been placed at extremely high-altitude sites ($\sim$5000 m) in dry, arid, mountainous deserts, to minimize the water column they have to observe through. These observations must still be corrected for the distortion of the signals by the atmosphere, by the use of accurate atmospheric models and calibration.

Early observations of circumstellar emission lines used single-dish telescopes, including the Onsala 20-m telescope, the Swedish-ESO Submillimetre Telescope (SEST), and the IRAM 30-m telescope. More recently, telescopes like APEX have enabled single-dish observations of higher sensitivity at sub-

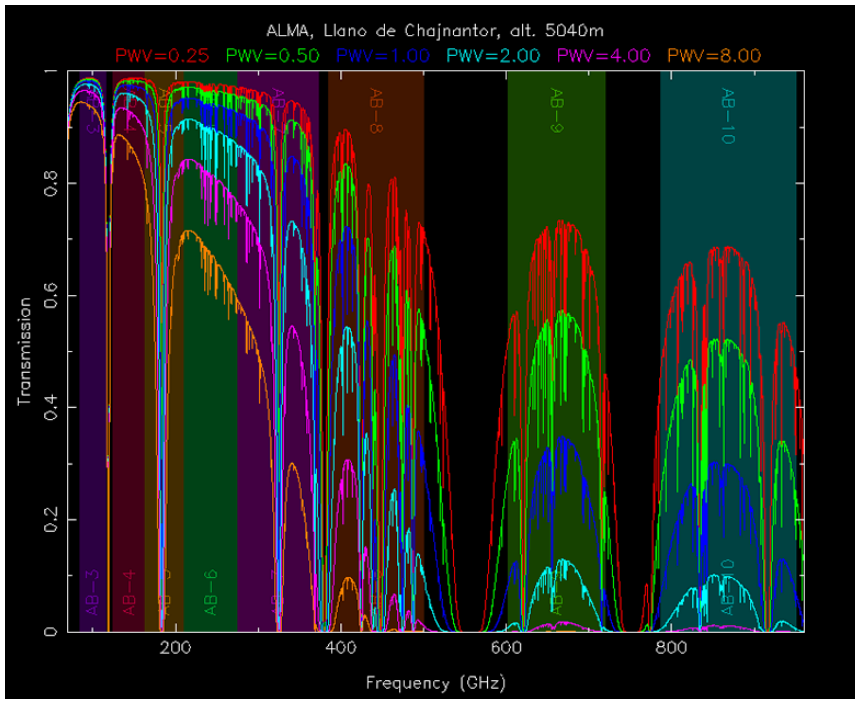

Figure 5.2: Atmospheric transmission at the ALMA site, for different PWVs. The vertical colour shadings denote the frequency ranges of the various ALMA bands (credit: ALMA Observatory).

mm/mm wavelengths. However, these telescopes, while providing extremely valuable information about the sources, could only obtain the spectra of the emission lines, and could not resolve the spatial distribution of the emitting regions. Interferometry using telescopes like ALMA and the Northern Extended Millimeter Array (NOEMA) has made it possible to spatially resolve and map the distribution of the emission, revolutionizing the field of sub-mm/mm astronomy. This project makes use of both single-dish and interferometric data observed using APEX, and ALMA, respectively. This chapter is a concise overview of the basic technical and scientific aspects of these observing techniques and telescopes.

5.2 Single-dish observations

A radio or sum-mm/mm telescope consists of an antenna and a receiver, used to capture electromagnetic waves coming from astronomical sources. The emission from astronomical sources is not easily detected, owing to their low intensities, and needs to be amplified. Contemporary single-dish telescopes like APEX employ heterodyne receivers, which are instruments comprised of a mixer, a set of amplifiers, filters, and finally a spectrometer. The mixer is used to convert the incoming high-frequency signal to a more easily-amplifiable lower frequency signal, by mixing the sky signal of frequency $f_{\rm sky}$) with a signal of frequency $f_{\rm LO}$ generated by the local oscillator (LO). This is done because amplification is much more easily possible for a lower-frequency signal. The mixers used in the receivers of APEX (and ALMA) are superconductor-insulator-superconductor (SIS) mixers, which offer high tunability and low noise in the sub-mm/mm range.

The intermediate frequency ($f_{\rm IF}$) is the frequency at which the incoming signal will be recorded by the spectrometers and is defined as:

$$f_{\rm IF} = |f_{\rm LO} - f_{\rm sky}| \tag{5.1}$$

The IF frequency can only be varied within specific limits for each instrument, which determine the bandwidth of the instrument. The IF signal includes two sidebands, as seen from Eq. 5.1, one on each side of the LO frequency. These sidebands are named the lower sideband (LSB), on the lower end of the LO frequency, and the upper sideband (USB), on its higher end. There are three modes of receiver operation, based on which signal from the respective sidebands is retained or suppressed. Sideband suppression is achieved by the use of selective filters next to the mixer. When only one of the sidebands is retained and the other is suppressed, the receiver is said to work in single sideband (SSB) mode. When both sidebands are retained, but superposed in the output spectrum, the receiver is said to operate in double sideband (DSB) mode. When both sidebands are retained and also separated in the final spectrum, the receiver mode is called sideband separated, or dual sideband (2SB).

The signal in the sideband(s) is then amplified using a cascade of low-noise amplifiers, so that the receiver output has high signal-to-noise ratio. The spectrometers record the intensity as a function of frequency, in bins of specified

width, the frequency resolution. Different spectrometers on the telescope can also process copies of the amplified signal simultaneously, without leading to reduced sensitivity. The intensity of the signal is expressed as an antenna temperature ($T_{\rm A}$). After calibrating for the atmospheric distortion and correcting for instrumental losses, the corrected antenna temperature is denoted by $T_{\rm A}^*$. The calibration process can be done in various ways. To remove the sky background, the *switching* methods usually employed during observations are:

- **Position switching**: repeatedly changing the pointing of the primary mirror between the source (ON) position and a noise-only (OFF) position, at regular intervals.
- **Beam switching**: repeatedly changing the pointing of the sub-reflector between the source (ON) position and a noise-only (OFF) position, at regular intervals.
- **Frequency switching**: repeatedly changing the LO frequency by a very small amount, at regular intervals. This method is very rarely used for observations of evolved stars.

The *chopper wheel* method, i.e. alternately observing a hot load (of ambient temperature), and then the cold sky, is employed for the flux calibration of sub-mm/mm single-dish telescopes.

As shown in Fig. 5.3 the *beam pattern* of a telescope antenna is characterised by a *main beam* and multiple *sidelobes*, indicating that all of the power received is not in the main beam. To estimate the power received in the main beam only, the main beam efficiency is defined as:

$$\eta_{\rm MB} = \frac{\Omega_{\rm MB}}{\Omega_{\rm total}} \tag{5.2}$$

where $\Omega_{\rm MB}$ is the solid angle of the main beam, and $\Omega_{\rm total}$ is the total solid angle of the antenna. Using this, we can convert the corrected antenna temperature ($T_{\rm A}^*$) to a main beam temperature ($T_{\rm MB}$) scale, as:

$$T_{\rm MB} = \frac{T_{\rm A}^*}{\eta_{\rm MB}} \tag{5.3}$$

This is the intensity scale mainly used in astrophysical calculations using single-dish data.

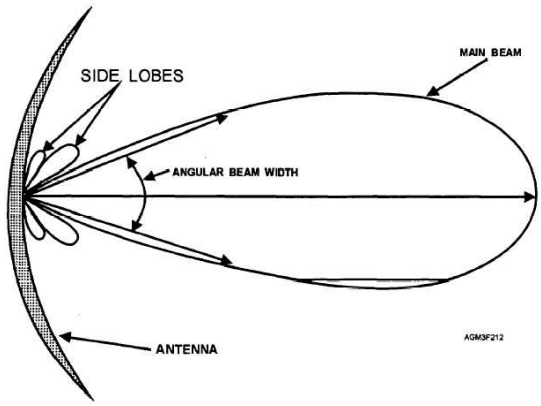

Figure 5.3: Polar plot of an antenna beam pattern, showing the main beam and sidelobes (credit: Argelander-Institut für Astronomie).

5.2.1 The APEX telescope

The Atacama Pathfinder Experiment (APEX[1], Güsten et al. 2006, Fig. 5.4), is a 12-m telescope operating at millimetre and sub-millimetre wavelengths, located at ∼5000 m altitude in the Chajnantor plateau in the Chilean Andes, one of the driest places on the planet. It is currently the largest sub-mm/mm telescope in the southern hemisphere, and can observe a range of astronomical sources and phenomena, from nearby stars and nebulae, to galaxies and cold clouds in the distant universe.

APEX currently hosts four facility instruments and seven PI instruments, ranging from large-aperture bolometers (e.g. *ArTéMiS*, Revéret et al. 2014) to heterodyne receivers (e.g. *SEPIA*, Belitsky et al. 2018). In addition, it can also host visitor instruments (e.g. *CONCERTO*, CONCERTO Collaboration et al. 2020). APEX was inaugurated in 2005, and is operated by a collaboration between the Max Planck Institute for Radio Astronomy (MPIfR) in Bonn, Germany, the European Southern Observatory (ESO), and the Onsala Space Observatory (OSO) in Sweden.

This project uses data obtained with APEX, observed using the following

[1] APEX is a collaboration between the Max Planck Institute for Radio Astronomy (MPIfR Bonn, Germany), the European Southern Observatory (ESO), and the Onsala Space Observatory (OSO), Sweden.

Figure 5.4: APEX gazing into the cosmos (credit: Babak Tafreshi, ESO)

receivers: SEPIA band 5 (159 - 211 GHz, Belitsky et al. 2018), PI230[2] (200 - 270 GHz), and SHeFI (200 - 270 and 272 - 376 GHz, Vassilev et al. 2008). See Sect. 3.1 of paper **??** for a detailed description of the observations.

5.3 Radio interferometry

The contents of this section are broadly based on Wilson et al. (2013) and Thompson et al. (2017), which serve as the general references wherever other literature is not explicitly cited.

The basic introduction to the theory and practice of interferometry presented in this section is far from complete, and is intended only as a simplistic overview of the bare minimum of its demanding concepts. A more detailed analysis of radio interferometry is outside the scope and intention of this thesis. Extensive literature is available on the topic, that the curious reader may refer to, including but not limited to Born & Wolf (1999); Taylor et al. (1999); Wilson et al. (2013) and Thompson et al. (2017).

[2]PI230 is a collaboration between the European Southern Observatory (ESO) and the Max-Planck-Institut für Radioastronomie (MPIfR).

Single-dish telescopes, while being very useful observing tools, have several limitations. As mentioned before, the mapping of the spatial distribution of the observed emission is not easily possible using single-dishes. Although they can be used to produce mosaic maps, this is still limited in terms of resolution and sensitivity. The angular resolution of a telescope is related to the wavelength of observation (λ), and the diameter (D) of the telescope, as:

$$\theta_{\rm res} \propto \frac{\lambda}{D} \tag{5.4}$$

This means that, for a given wavelength, the angular resolution is better for a larger telescope. Also, for long-wavelength observations, very large-diameter telescopes are required to achieve the same angular resolution as a smaller telescope has at shorter wavelengths. Even though very large-aperture single-dish telescopes like the Five hundred meter Aperture Spherical Telescope (FAST), and the Arecibo observatory have been built, practical constraints make the construction of larger and larger single-dish telescopes impossible, and they also become increasingly less flexible in the ways they can observe, as their aperture size increases. It is to overcome this limitation that the technique of radio interferometry was developed.

Radio interferometers work based on the principle that a resolution of $\theta_{\rm res}$ obtained by a single-dish of diameter D can also be obtained by combining the signal received by two antennas of smaller diameter, ($d \ll D$, see Fig. 5.5) but separated by a distance D (see Born & Wolf 1999). This means that the angular resolution of an interferometer is limited not by the diameters of the individual antennas, but by the largest separation between two dishes. The separations between the antennas of an interferometer are known as baselines.

This technique can be extended to a multi-antenna system which can produce high-resolution images of the sky, by combining independent observations of pairs of antennas spread over the equivalent aperture. This is known as aperture synthesis. The angular resolution of an aperture synthesis interferometer is given by:

$$\theta_{\rm res} = \frac{\lambda}{|\mathbf{b}|} \tag{5.5}$$

where $|\mathbf{b}|$ is the length of the longest baseline. Increasingly finer structures can be resolved by increasing $|\mathbf{b}|$. It is to be noted that the "equivalent aperture" generated by an interferometer, albeit offering high spatial resolution,

is not filled, and this affects the sensitivity of the observations.

5.3.1 Observing with a radio interferometer

A block diagram of a simple 2-element interferometer is shown in Fig. 5.5. The two antennas are separated by a baseline separation **b**, and are connected to a correlator which multiplies and time-averages the signals from the two antennas.

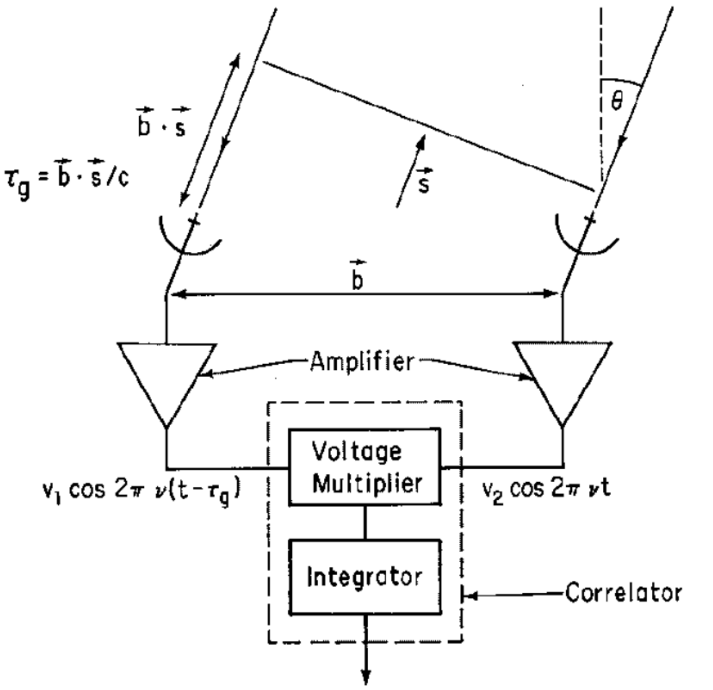

Figure 5.5: Block diagram of a 2-element interferometer. τ_g is the geometric delay between the times at which the two antennas receive signal from the far-away astronomical source in the direction **s** (credit: Thompson, in Taylor et al. 1999).

When we observe an astrophysical phenomenon happening at location **R** in space, what we are effectively doing is to record the time-varying electric field

($\mathbf{E}(\mathbf{R}$,t)) which propagates to us from that point. We can write the magnitude of this electric field as a sum of Fourier components. The fourier coefficients ($\mathbf{E}_\nu(\mathbf{R})$) thus obtained are complex quantities. However, the propagated components of the electric field at the observer's location, say $\mathbf{E}_\nu(\mathbf{r})$ is what is observable to us. Of particular interest to interferometry is the *correlation* of the electric fields at two observing points, say $\mathbf{r}_1$ and $\mathbf{r}_2$. This is calculated by the *correlator* (Fig. 5.5) of the interferometer. Under the reasonable simplifying assumptions that the radiating source is very far away, and that the emission from two different points in space is spatially incoherent, we can write this correlation as an integral of the observed intensity (I_ν) over solid angle (see Clark, in Taylor et al. 1999), as:

$$V_\nu(\mathbf{r}_1, \mathbf{r}_2) = \int I_\nu(\mathbf{s}) e^{-2\pi i \nu \mathbf{s}\cdot(\mathbf{r}_1 - \mathbf{r}_2)/c} d\Omega \tag{5.6}$$

where $\mathbf{s}$ is the unit vector in the direction of the source, and c is the speed of light. It can be seen that Eq. 5.6 depends only on the separation between the two observing points ($\mathbf{r}_1$ - $\mathbf{r}_2$), and not on their absolute positions. The function $V_\nu(\mathbf{r}_1,\ \mathbf{r}_2)$ is known as the *spatial correlation function* of the field components. Also, Eq. 5.6 can be inverted to find the intensity distribution of the emitting source. The interferometer is an instrument to measure the values of this function.

If we define the coordinate system describing the baseline separations ($\mathbf{r}_1$ - $\mathbf{r}_2$) as (u, v), measured in units of wavelength (λ), and set the components of the sky coordinates ($\mathbf{s}$) to be described by the unit vectors (l, m), we can rewrite Eq. 5.6 as:

$$V_\nu(u, v) = \iint A_\nu(l, m) I_\nu(l, m) e^{-2\pi i(ul + vm)} dl dm \tag{5.7}$$

where a normalising factor, A_ν(l, m), has also been included to account for the directional sensitivity of the antenna reception. This quantity, $V_\nu(u, v)$, is known as the *complex visibility function*, and has an amplitude and a phase. The fundamental principle of radio interferometry, the *van Cittert-Zernike theorem*, states that the complex visibility function is the Fourier transform of the brightness distribution of the source in the sky (see Thompson, Moran, and Swenson, in Thompson et al. 2017).

The sampling of the uv plane can be increased for a given baseline configuration by making use of the fact that the Earth's rotation constantly changes

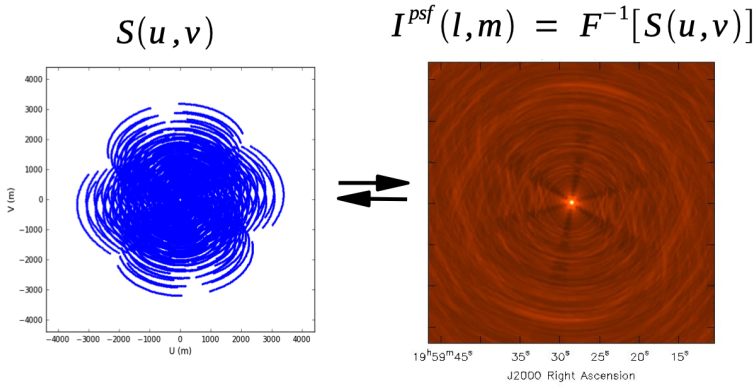

Figure 5.6: A typical *uv* coverage (left) and the corresponding PSF (right) of a modern radio interferometer (credit: NRAO).

the effective direction of the baseline vectors. This process is known as *Earth rotation synthesis*. Even then, as a practical interferometer can never sample the *uv* plane entirely, as it can have only a limited number of discrete baselines, the inversion of this equation will not provide the exact emission distribution in the sky, but only one which is convolved with the Fourier transform of the sampling function ($S(u, v)$) of the array (see Clark, in Taylor et al. 1999), i.e.,

$$I_\nu^D(l,m) = \iint V_\nu(u,v) S(u,v) e^{2\pi i(ul+vm)} du dv \tag{5.8}$$

where $I_\nu^D(l, m)$ is called the *dirty image*, which is a convolution of the point spread function (PSF) or *synthesised beam* ($B(l, m)$, the Fourier transform of $S(u, v)$) with the actual source intensity distribution ($I_\nu(l, m)$).

$$I_\nu^D(l,m) = I_\nu^{sky}(l,m) * B(l,m) \tag{5.9}$$

Fig. 5.6 shows a typical *uv* coverage and PSF of a modern radio interferometer. The dirty image is contaminated by the sidelobes of the PSF. The purpose of all interferometric imaging algorithms is the iterative Fourier inversion of the observed visibilities to produce the dirty image (Eq. 5.8), and the deconvolution of the beam from the dirty image to obtain the true source distribution. This process is known as *cleaning*, and algorithms like *clean* (Högbom 1974), *maximum entropy method* (MEM, Cornwell & Evans 1985),

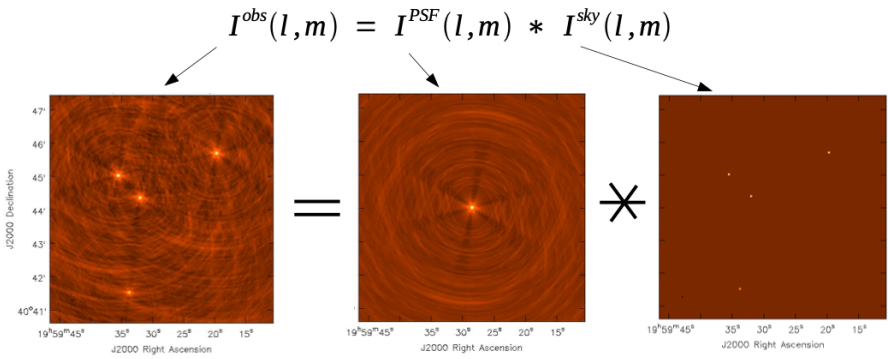

Figure 5.7: The observed (dirty) image, the PSF, and the actual sky distribution of a typical interferometric observation, visually depicting the convolution given in Eq. 5.9 (credit: NRAO).

multi-frequency synthesis (MFS, Conway et al. 1990), and *multiscale tclean* (Cornwell 2008) have been developed for this purpose. The observed (dirty) image, the PSF, and the actual sky distribution of a typical interferometric observation are shown in Fig. 5.7.

Different weighting schemes can be used to assign weights to visibilities while imaging, to suppress or enhance artefacts/features as necessary. These include *natural weighting*, where all visibilities have the same weight, resulting in the best possible signal-to-noise ratio but poorer angular resolution, and *uniform weighting*, where each measured spatial frequency is given the same weight, irrespective of its sampling density, resulting in higher angular resolution. Additionally, the *Briggs weighting* scheme (Briggs 1995) can be used to balance the trade-off between signal-to-noise ratio and angular resolution, using an adjustable *robustness* parameter, which can take values between -2 (close to uniform weighting) and 2 (close to natural weighting). The weighting scheme used for the images presented in paper **??** is Briggs weighting, with a robustness parameter of 0.5.

5.3.2 Calibration

The visibilities observed by an interferometer need not exactly equal the true sky visibilities, as multiple factors, including atmospheric and instrumental

distortions will introduce errors in the observed quantities. The ratio of the observed visibilities to the true visibilities is known as the *complex gain* of the interferometer. Based on their origin, gains can be frequency- and/or time-dependent. The process of estimating the true visibilities from the observed ones, by correcting for the various gains, is known as calibration.

There are a variety of calibration steps that need to be applied to the visibility data, before it is ready for imaging. First, corrections for instrumental errors like those in pointing and antenna positions are applied to the observed data. This is followed by three major calibration processes, namely bandpass calibration, phase calibration, and flux calibration. To enable these calibrations to be performed, calibrator sources, whose flux and position are well known, mostly quasars or solar system objects, are observed at specific intervals in between the science target observations.

Bandpass calibration compensates for the variation of the antenna gains with frequency, by applying the gain solutions calculated to flatten the observed spectrum of the bandpass calibrator to the science target. The bandpass calibrator has to be a source with a flat spectrum, or a known spectral index.

Phase calibration corrects the frequency-independent gains, i.e., it compensates for the relative time variations in the phase of the correlated signal, caused by the atmosphere. Phase calibration is hence crucial to recover the source structure in the sky. The phase calibrator has to be a point source (i.e. zero phase), or an object with a precisely known source structure, located close to the science target in the sky, so that the atmosphere is roughly the same towards both.

Flux calibration is used to set the amplitude scales of the observed intensity. It also compensates for the atmospheric opacity and instrumental signal loss. The flux calibrator needs to be a source for which an accurate, independently calibrated flux model exists, typically a well-monitored quasar. Previously, solar system objects like planets and asteroids were also used as flux calibrators. Errors in calibration, for example those caused by badly modelled flux calibrators, can lead to artefacts in the final images, as discussed in Sect. 3.2 of paper **??**.

Self-calibration is another method of correcting the phase errors, but at smaller timescales than that of phase calibration, by using a sky model created from bright, compact emission (like a compact continuum) from the

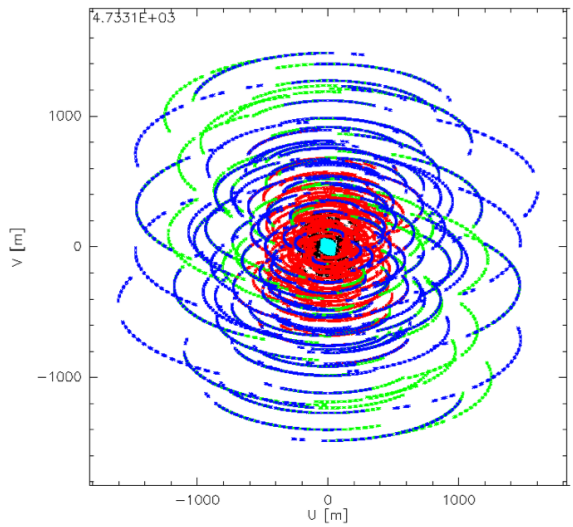

Figure 5.8: Combination of visibilities from different baseline configurations, shown in the *uv* plane. The red points indicate compact baselines, while the green adn blue points show successively extended array configurations (credit: NRAO).

science target itself, rather than a separate calibrator source. This gives the added advantage that the assumption during normal phase calibration that the atmospheric variations are the same towards the calibrator and the target, is no longer required. Self-calibration is a very powerful technique, but may or may not provide significant improvements in sensitivity, depending on the compactness and strength of the emission chosen to create the model, and the timescales of the leftover phase variations present in the calibrated *uv* data. In paper **??**, self-calibration was attempted on several tunings of the ALMA data, but did not result in any noticeable improvement in the final images.

5.3.3 Data combination

It is possible to combine multiple interferometric observations performed towards a source by concatenating the visibilities from the different observations.

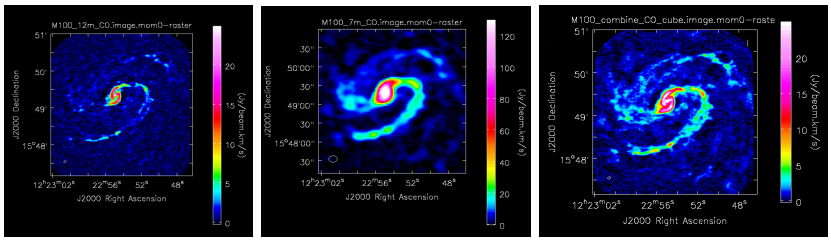

(a) 12-m array image **(b)** 7-m array image **(c)** Combined image

Figure 5.9: Images of the CO(1-0) emission from the galaxy M100, (a) using the ALMA main array, (b) using the ACA, and (c) using combined data from ALMA main array and ACA. Note the increased fidelity in the combined image (credit: NRAO).

This leads to a better sampling of the *uv* plane, and therefore to images of better fidelity and sensitivity. It is also possible to concatenate data from different arrays of an interferometer, for e.g. the 12-m and 7-m arrays of ALMA (see Sect. 5.3.4). The combination of visibilities from different baseline configurations in the *uv* plane is shown in Fig. 5.8. Fig. 5.9 shows the ALMA images of the barred spiral galaxy M100 in CO(1-0) line emission, before and after data combination.

For paper **??**, two different ALMA datasets, both from the main (12-m) array, but with different array configurations, were combined (see Sect. 3.3 of paper **??**). This significantly improved the quality of the resulting images, both in terms of angular resolution and sensitivity, and led to the detection of several weak emission lines.

5.3.4 The ALMA observatory

The Atacama Large Millimeter/sub-millimeter Array (ALMA[3], Fig. 5.10), is a 66 antenna sub-mm/mm aperture synthesis interferometer, located at ∼5000 m altitude in the Chajnantor plateau in Chile, close to the APEX telescope. The extremely dry atmosphere and the high altitude of Chajnantor offer excellent conditions for high-sensitivity sub-mm/mm observations.

[3]ALMA is a partnership of ESO (representing its member states), NSF (USA) and NINS (Japan), together with NRC (Canada), MOST and ASIAA (Taiwan), and KASI (Republic of Korea), in cooperation with the Republic of Chile.

Figure 5.10: An excited observer at the ALMA site (photo by Mamiko Sato)

ALMA has been operating since 2011, and it is currently the largest sub-mm/mm interferometer in the world, and one of the most complicated scientific instruments ever built. It consists of two arrays, with fifty 12-m antennas forming the ALMA main array, complemented by the twelve closely-spaced 7-m antennas of the Atacama Compact Array (ACA), also known as the Morita array. In addition, it also has four single-dish or total-power (TP) antennas. It currently has 8 observing bands, together covering the frequency range of 84−950 GHz, with some interruptions in between. Two more bands are under construction, which will extend the observing capabilities down to 35 GHz in the near future. ALMA can observe in only one band at any given time. Each receiver band can detect two orthogonal linear polarizations. Bands 3 to 8 are dual-sideband (2SB, Sect. 5.2), while bands 9 and 10 are double-sideband (DSB, Sect. 5.2). See the ALMA technical handbook[4] for more specifications and details of the ALMA antennas, receivers, and bands.

[4] https://almascience.eso.org/documents-and-tools/cycle9/alma-technical-handbook

The antennas of the ALMA array can be arranged in different baseline configurations across the 192 antenna foundations, to perform observations aimed to recover emission at various spatial scales. The minimum and maximum baselines obtainable are 15 m and ∼16 km respectively, enabling ALMA to observe at a broad range of spatial scales and resolutions. This work has used ALMA observations in Band 3 (84-116 GHz). The minimum and maximum baselines, beam sizes, spectral resolutions, and other observational details of the data used in this project are listed in Table 2 of paper **??**.

6

Summary of Paper A

Paper **??** presents the analysis and results of the spatially-resolved ALMA band 3 (84−116 GHz) spectral survey observations of three C-rich AGB stars, IRAS 15194−5115, IRAS 15082−4808, and IRAS 07454−7112. We attempt to compare and contrast the chemistry in their CSEs with that of the well-studied C-star IRC +10 216, aiming to put to test the archetype C-star status often attributed to it in the literature. It is aimed at producing a more generalised understanding of the physical and chemical characteristics of carbon-rich AGB CSEs, which is currently lacking. These are the first high spatial-resolution observations of the circumstellar molecular emission from a sample of carbon stars other than IRC +10 216, across large bandwidths.

The paper is divided into five sections. The general introduction in Sect. 1 lists the existing literature on the subject, outlining the necessity of the present study. Following this, the properties of the chosen sources and the reasons for their selection are described in Sect. 2. The stars present similar physical outflow properties, possessing roughly spherical CSEs with similar expansion velocities. They trace around an order of magnitude in mass loss rates, from 3×10^{-6} to around 1.6×10^{-5} $M_{\odot}$ yr^{-1}. However, they have very different $^{12}C/^{13}C$ ratios, indicative of differences in their nucleosynthetic his-

tories. Thus, they are ideal candidates for a comparative study of carbon-rich circumstellar envelopes.

The details of the observations, and data reduction methods used are described in Sect. 3. We observed the three sources in the full bandwidth of ALMA band 3 (84-116 GHz), using the main array (12 m) antennas. Sect. 3.2 describes the recalibration and re-imaging that had to be performed on the archival data due to its poor quality. The data combination process employed to combine parts of our dataset with a subset of overlapping frequency range data from another ALMA project obtained from the archive is discussed in Sect. 3.3.

The scientific analysis employed, along with the results obtained are presented in Sect. 4. The survey yielded 311 identified lines, including hyperfine splitting components, from 141 transitions of 49 molecular species and their various isotopologues. We report multiple new detections towards the stars in the sample, including ^{29}SiO, ^{30}SiO, ^{29}SiS, ^{30}SiS, Si^{34}S, C^{33}S, Si^{13}CC, C_6H, C_8H, l$-C_4H_2$, and doubly ^{13}C−substituted isotopologues of HC_3N.

Two main morphological categories are found in the line emission maps of molecules, namely *centrally-peaked* emission (HCN, SiO, SiS, and CS), and emission from a *shell* (C_2H, C_3H, C_4H, c-C_3H_2, CN, C_3N, HC_5N, and HNC). Two species, HC_3N and SiC_2, present more complex brightness distributions characterised by both central and shell components. In addition, for IRAS 15194−5115 and IRAS 15082−4808 deviations from a smooth spherical CSE are evident as multiple well-resolved arc-like structures traced by several species. These CSEs display complex structures, possibly indicative of the presence of binary companions.

We determined the spatial extents of the emission from various molecules from the resolved emission maps, by producing azimuthally averaged radial profiles (AARPs) of the systemic-velocity emission and fitting them with Gaussians. We compared the radial order of appearance of various molecules in our stars to that of IRC +10 216, and find them to be roughly the same. This is an advantage of having spatially-resolved emission maps, in contrast to single-dish spectra, that the radial order of the emitting regions of different molecules, which is directly correlated with CSE chemistry, can be directly visualised. The calculated emission extents were used to calculate LTE estimates of molecular abundances. For molecules with three or more detected transitions sufficiently well-separated in upper-level energies, we employed the

population diagram method (Sect. 4.2.1) to estimate the abundances. For other species, we present approximate analytical estimates of fractional abundances, produced using assumed excitation temperatures. Within the uncertainties of the data and analysis, we find that the calculated abundances are very similar among our sources and IRC +10 216. These indicate that the general chemistry in these objects is highly similar.

We also estimated the isotopic ratios of silicon and sulphur in the envelopes, and they match reasonably well with the typical expected AGB values. The $^{12}C/^{13}C$ ratios were also calculated for each envelope, from multiple molecules, and were found to conform very well to the values in the literature.

Sect. 5 discusses the relevance and implications of our results. Overall, we conclude that the chemistry in the three envelopes is very similar to one another and to IRC +10 216, both in terms of the radial extents of the emission from various species, and molecular abundances. Detailed radiative transfer modelling is required to more rigorously constrain the molecular abundances. These, along with the subsequently updated chemical models, will be presented in upcoming papers.

7

Outlook and future work

7.1 Overview of planned work

Even though the LTE analysis employed in paper **??** to estimate circumstellar molecular abundances is a useful first step, it is not without its limitations. The methods used, including population diagrams, assume that the molecules are in local thermodynamic equilibrium (LTE), which need not always be the case throughout the envelope. The proper treatment of molecular excitation, taking into account non-LTE conditions and optical depth effects, calls for detailed radiative transfer analysis. Given that the comparison of molecular abundances across the sample is a key aspect of this work, it is important to obtain more accurate abundance estimates, which is only possible using radiative transfer analysis. Such a study is outside the scope of the work presented in paper **??**, and shall be presented in an upcoming paper, where a selection of species from the detected molecules will be analysed using radiative transfer modelling.

Single-dish spectral surveys that cover a much larger wavelength range that the ALMA data presented in paper **??** have already been observed and are available locally. All three sources presented in paper **??**, and also AFGL

3068 and also IRC 10 216 itself have APEX spectra (159 - 270 GHz) available. In addition, Herschel/HIFI spectra, and higher frequency APEX spectra (272 - 376 GHz) are available for IRAS 15194−5115. The wealth of emission line information extracted from these datasets will allow us to comprehensively explore a broader range of excitation conditions prevalent in AGB CSEs. These datasets will be presented in detail in an upcoming paper, and will also serve as additional inputs to the radiative transfer models. The results from the radiative transfer analysis will be used to inform the updation of the existing chemical models of AGB CSEs, and also to provide a more accurate comparison of the molecular abundances across the sample.

More work is planned to be done on the observational front as well, to follow up the results of the current work. As discussed in paper **??**, the arc structures seen in the emission maps of several molecules indicate density enhancements potentially caused by the presence of binary companions. The proper characterisation of the observed complex morphologies, and detailed investigations into the presence of potential binary companions demand observations of higher angular resolution and sensitivity.

7.2 Outlook

The scope of the current and planned work, as mentioned above, is limited to the study of carbon-star CSEs. The extension of such comparative analysis into the regime of M-type and S-type AGB stars is a logical next step. Only with such coordinated studies across the different AGB types can we hope to comprehensively understand the complex chemical evolution taking place in this phase of stellar evolution. Expanding the molecular inventories of circumstellar material across the fundamentally different types of evolved stars also opens up interesting possibilities of tracing the chemical evolution of whole galaxies.

Although an overall, broad understanding of the physics and chemistry on the AGB has been established (e.g. Habing & Olofsson 2003; Höfner & Olofsson 2018) and is being regularly updated through extensive modelling and observations, there are still many aspects of the AGB phase that are yet to be completely understood. Explaining the mass loss mechanism from first principles to develop a predictive theory of AGB mass loss, and characterising the nature and extent of the various complex chemical pathways and processes

taking place in circumstellar envelopes, are just two major examples. The observations presented in this work, and the upcoming radiative transfer and chemical modelling can contribute significantly towards the latter, offering new insights into the chemical evolution occurring during the AGB.

Recent advances in our observing capabilities, such as the development of the Atacama Large Millimeter/submillimeter Array (ALMA), the James Webb Space Telescope (JWST), and the upcoming Square Kilometre Array (SKA) are opening up new and exciting avenues for the future of AGB research. ALMA now allows us to probe the molecular chemistry of AGB CSEs in unprecedented spatial resolution and sensitivity, revealing complex morphological structures and leading to the detection of more and more molecular species. The JWST will provide us with the opportunity to study the dust around AGB CSEs in the infrared, while also making the photometry and spectroscopy of AGB stars in nearby galaxies easier (e.g. Meixner 2011; Eriksson et al. 2014). The SKA will study the dynamical atmospheres of AGB stars in radio, unveiling the origin of their stellar winds and exploring their dust-formation zones. Together, these instruments will allow us to explore the AGB in a broad range of wavelengths, and potentially obtain a more comprehensive picture of these fantastic objects.

Bibliography

Agúndez, M., Cernicharo, J., Quintana-Lacaci, G., et al. 2017, A&A, 601, A4

Agúndez, M., Fonfría, J. P., Cernicharo, J., et al. 2012, A&A, 543, A48

Allain, T., Sedlmayr, E., & Leach, S. 1997, A&A, 323, 163

Andriantsaralaza, M., Ramstedt, S., Vlemmings, W. H. T., & De Beck, E. 2022, A&A, 667, A74

Belitsky, V., Lapkin, I., Fredrixon, M., et al. 2018, A&A, 612, A23

Blommaert, J. A. D. L., de Vries, B. L., Waters, L. B. F. M., et al. 2014, A&A, 565, A109

Blommaert, J. A. D. L., Groenewegen, M. A. T., Okumura, K., et al. 2006, A&A, 460, 555

Bodenheimer, P. H. 2011, Principles of Star Formation

Born, M. & Oppenheimer, R. 1927, Annalen der Physik, 389, 457

Born, M. & Wolf, E. 1999, Principles of Optics

Bowen, G. H. 1988, ApJ, 329, 299

Briggs, D. S. 1995, High fidelity deconvolution of moderately resolved sources, PhD thesis, New Mexico Institute of Mining and Technology

Brown, J. M. & Millar, T. J. 2003, MNRAS, 339, 1041

Bujarrabal, V., Fuente, A., & Omont, A. 1994, A&A, 285, 247

Cernicharo, J., Guélin, M., & Kahane, C. 2000, A&AS, 142, 181

Cernicharo, J., Waters, L. B. F. M., Decin, L., et al. 2010, A&A, 521, L8

Cherchneff, I. 2006, A&A, 456, 1001

Cherchneff, I., Barker, J. R., & Tielens, A. G. G. M. 1992, ApJ, 401, 269

CONCERTO Collaboration, Ade, P., Aravena, M., et al. 2020, A&A, 642, A60

Conway, J. E., Cornwell, T. J., & Wilkinson, P. N. 1990, MNRAS, 246, 490

Cordiner, M. A. & Millar, T. J. 2009, ApJ, 697, 68

Cornwell, T. J. 2008, IEEE Journal of Selected Topics in Signal Processing, 2, 793

Cornwell, T. J. & Evans, K. F. 1985, A&A, 143, 77

Danilovich, T., De Beck, E., Black, J. H., Olofsson, H., & Justtanont, K. 2016, A&A, 588, A119

Danilovich, T., Richards, A. M. S., Decin, L., Van de Sande, M., & Gottlieb, C. A. 2020, MNRAS, 494, 1323

Danilovich, T., Richards, A. M. S., Karakas, A. I., et al. 2019, MNRAS, 484, 494

De Beck, E., Lombaert, R., Agúndez, M., et al. 2012, A&A, 539, A108

De Beck, E. & Olofsson, H. 2018, A&A, 615, A8

De Beck, E. & Olofsson, H. 2020, A&A, 642, A20

Dinh-V-Trung & Lim, J. 2008, ApJ, 678, 303

Dorschner, J. 2010, in Lecture Notes in Physics, Berlin Springer Verlag, ed. T. Henning, Vol. 815, 1–60

Eriksson, K., Nowotny, W., Höfner, S., Aringer, B., & Wachter, A. 2014, A&A, 566, A95

Fonfría, J. P., DeWitt, C. N., Montiel, E. J., Cernicharo, J., & Richter, M. J. 2022, ApJ, 927, L33

Gail, H.-P. & Sedlmayr, E. 2013, Physics and Chemistry of Circumstellar Dust Shells

Gobrecht, D., Cherchneff, I., Sarangi, A., Plane, J. M. C., & Bromley, S. T. 2016, A&A, 585, A6

Groenewegen, M. A. T., Barlow, M. J., Blommaert, J. A. D. L., et al. 2012, A&A, 543, L8

Guélin, M., Patel, N. A., Bremer, M., et al. 2018, A&A, 610, A4

Güsten, R., Nyman, L. Å., Schilke, P., et al. 2006, A&A, 454, L13

Habing, H. J. & Olofsson, H. 2003, Asymptotic giant branch stars

He, J. H., Dinh-V-Trung, Kwok, S., et al. 2008, ApJS, 177, 275

Herwig, F. 2005, ARA&A, 43, 435

Höfner, S., Bladh, S., Aringer, B., & Ahuja, R. 2016, A&A, 594, A108

Höfner, S. & Olofsson, H. 2018, A&A Rev., 26, 1

Högbom, J. A. 1974, A&AS, 15, 417

Hron, J., Loidl, R., Hoefner, S., et al. 1998, A&A, 335, L69

Iben, I., J. 1975, ApJ, 196, 525

Iben, Icko, J. 1973, ApJ, 185, 209

Karakas, A. I. & Lattanzio, J. C. 2014, PASA, 31, e030

Karakas, A. I. & Lugaro, M. 2010, PASA, 27, 227

Kim, H., Liu, S.-Y., Hirano, N., et al. 2015, ApJ, 814, 61

Kippenhahn, R. & Weigert, A. 1990, Stellar Structure and Evolution

Kobayashi, C., Karakas, A. I., & Lugaro, M. 2020, ApJ, 900, 179

Kraemer, K. E., Sloan, G. C., Keller, L. D., et al. 2019, ApJ, 887, 82

Kwok, S. 2007, Physics and Chemistry of the Interstellar Medium

Lamers, H. J. G. L. M. & Levesque, E. M. 2017, Understanding Stellar Evolution

LeBlanc, F. 2010, An Introduction to Stellar Astrophysics

Li, X., Millar, T. J., Walsh, C., Heays, A. N., & van Dishoeck, E. F. 2014, A&A, 568, A111

Liljegren, S. 2018, Stellar winds of cool giants: Investigating the mass-loss mechanism of AGB Stars, PhD thesis, Uppsala University, Sweden

Maercker, M., Vlemmings, W. H. T., Brunner, M., et al. 2016, A&A, 586, A5

Markwick, A. J. 2000, Chemistry in dynamically evolving astrophysical regions, PhD thesis, University of Manchester, Institute of Science and Technology

Massalkhi, S., Agúndez, M., & Cernicharo, J. 2019, A&A, 628, A62

McGuire, B. A. 2022, ApJS, 259, 30

McKee, C. F. & Ostriker, E. C. 2007, ARA&A, 45, 565

Meixner, M. 2011, in Astronomical Society of the Pacific Conference Series, Vol. 445, Why Galaxies Care about AGB Stars II: Shining Examples and Common Inhabitants, ed. F. Kerschbaum, T. Lebzelter, & R. F. Wing, 555

Müller, H. S. P., Schlöder, F., Stutzki, J., & Winnewisser, G. 2005, Journal of Molecular Structure, 742, 215

Nyman, L. A., Olofsson, H., Johansson, L. E. B., et al. 1993, A&A, 269, 377

Olofsson, H., Eriksson, K., & Gustafsson, B. 1990, A&A, 230, 405

Olofsson, H., Lindqvist, M., Nyman, L. A., & Winnberg, A. 1998, A&A, 329, 1059

Pardo, J. R., Cernicharo, J., Tercero, B., et al. 2022, A&A, 658, A39

Patel, N. A., Young, K. H., Gottlieb, C. A., et al. 2011, ApJS, 193, 17

Revéret, V., André, P., Le Pennec, J., et al. 2014, in Society of Photo-Optical Instrumentation Engineers (SPIE) Conference Series, Vol. 9153, Millimeter, Submillimeter, and Far-Infrared Detectors and Instrumentation for Astronomy VII, ed. W. S. Holland & J. Zmuidzinas, 915305

Saberi, M., Vlemmings, W. H. T., & De Beck, E. 2019, A&A, 625, A81

Sackmann, I. J., Smith, R. L., & Despain, K. H. 1974, ApJ, 187, 555

Salaris, M. & Cassisi, S. 2005, Evolution of Stars and Stellar Populations

Schöier, F. L., Ramstedt, S., Olofsson, H., et al. 2013, A&A, 550, A78

Sedlmayr, E. & Dominik, C. 1995, Space Sci. Rev., 73, 211

Siess, L., Livio, M., & Lattanzio, J. 2002, ApJ, 570, 329

Sloan, G. C., Little-Marenin, I. R., & Price, S. D. 1998, AJ, 115, 809

Smith, C. L., Zijlstra, A. A., & Fuller, G. A. 2015, MNRAS, 454, 177

Stahler, S. W. & Palla, F. 2004, The Formation of Stars

Sugimoto, D. & Nomoto, K. 1975, PASJ, 27, 197

Taylor, G., Carilli, C., & Perly, R. 1999, in Astronomical Society of the Pacific Conference Series, Vol. 180, Synthesis Imaging in Radio Astronomy II

Thompson, A. R., Moran, J. M., & Swenson, George W., J. 2017, Interferometry and Synthesis in Radio Astronomy, 3rd Edition

Tielens, A. G. G. M. 2005, The Physics and Chemistry of the Interstellar Medium

Toonen, S., Hamers, A., & Portegies Zwart, S. 2016, Computational Astrophysics and Cosmology, 3, 6

Tosi, S., Dell'Agli, F., Huerta-Martinez, E., & Ventura, P. 2022, Universe, 8, 270

Unnikrishnan, R., De Beck, E., Nyman, L. Å., & Olofsson, H. in prep.

Unnikrishnan, R., De Beck, E., Nyman, L. Å., et al. 2023, Submitted to A&A

Van de Sande, M. & Millar, T. J. 2019, ApJ, 873, 36

Van de Sande, M., Walsh, C., & Danilovich, T. 2020, MNRAS, 495, 1650

Van de Sande, M., Walsh, C., Mangan, T. P., & Decin, L. 2019, MNRAS, 490, 2023

Van de Sande, M., Walsh, C., & Millar, T. J. 2021, MNRAS, 501, 491

Vassilev, V., Meledin, D., Lapkin, I., et al. 2008, A&A, 490, 1157

Vassiliadis, E. & Wood, P. R. 1993, ApJ, 413, 641

Velilla Prieto, L., Cernicharo, J., Agúndez, M., et al. 2019, A&A, 629, A146

Velilla Prieto, L., Cernicharo, J., Quintana-Lacaci, G., et al. 2015, ApJ, 805, L13

Velilla Prieto, L., Sánchez Contreras, C., Cernicharo, J., et al. 2017, A&A, 597, A25

Ventura, P., Dell'Agli, F., Schneider, R., et al. 2014, MNRAS, 439, 977

Ward-Thompson, D. & Whitworth, A. P. 2011, An Introduction to Star Formation

Willson, L. A. 2000, ARA&A, 38, 573

Wilson, T. L., Rohlfs, K., & Hüttemeister, S. 2013, Tools of Radio Astronomy

Wood, P. R. 1979, ApJ, 227, 220

Woods, P. M., Schöier, F. L., Nyman, L. Å., & Olofsson, H. 2003, A&A, 402, 617

Zijlstra, A. A., Matsuura, M., Wood, P. R., et al. 2006, MNRAS, 370, 1961